Geologic interpretations of seismic scattering and attenuation for the Cianten Caldera and the surrounding area

by

Clarion Hadleigh Hess

Submitted to the Department of Earth, Atmospheric, and Planetary Sciences
in partial fulfillment of the requirements for the degree of

Master of Science in Geophysics

at the

MASSACHUSETTS INSTITUTE OF TECHNOLOGY

June 2013

Author .....
Department of Earth, Atmospheric, and Planetary Sciences
May 30, 2013

Certified by .....
Professor Alison Malcolm
Atlantic Richfield Career Development Assistant Professor,
Department of Earth, Atmospheric, and Planetary Sciences
Thesis Supervisor

Accepted by .....
Professor Robert D. van der Hilst
Schlumberger Professor of Earth Sciences,
Head, Department of Earth, Atmospheric, and Planetary Sciences

Geologic interpretations of seismic scattering and attenuation for the Cianten Caldera and the surrounding area

by

Clarion Hadleigh Hess

Submitted to the Department of Earth, Atmospheric, and Planetary Sciences
on May 30, 2013, in partial fulfillment of the
requirements for the degree of
Master of Science in Geophysics

Abstract

The Cianten Caldera in Indonesia is immediately adjacent to the producing portion of the Awibengkok geothermal field. The Cianten Caldera contains rocks similar to those in the Awibengkok field, however, the Cianten Caldera is not capable of producing geothermal power on a commercial scale. The Cianten Caldera has been microseismically monitored along with the producing Awibengkok field as injections and fracing in that field have occurred. This microseismic data is analyzed with Multi Window Time Lapse Analysis (MWTLA) to find values for the scattering coefficient, g_o, and the seismic albedo, B_o, of the Cianten Caldera. The scattering coefficient describes the amount of seismic energy that is attenuated due to the wave scattering off of heterogeneities and the seismic albedo is the ratio of the amount of scattering to the total amount of attenuation that includes both scattering and intrinsic attenuation. This information has been combined with the geology of the Cianten Caldera to define the interior features of the Cianten Caldera and which of these features are preventing the Cianten Caldera from being a productive geothermal energy source.

Thesis Supervisor: Professor Alison Malcolm
Title: Atlantic Richfield Career Development Assistant Professor, Department of Earth, Atmospheric, and Planetary Sciences

Acknowledgments

I would like to thank my advisor, Alison Malcolm, for all of her guidance during this project and her assistance in revising this thesis. I would also like to thank Gabi Melo for her help in the selection and quality control of the subset of data that was analyzed.

I would like to thank Chevron for the use of their microseismic data.

Contents

List of Figures

List of Tables

Chapter 1

Introduction

1.1 Motivation

Seismic observation is one of the few methods that can be used to observe material properties within the Earth. The seismic signals carry valuable information about the interior of the Earth since they are affected by variations in the medium that the wave travels through, including variations in porosity, pore fluids, density, composition, and chemical structure. Seismic observation can determine different geologic features including the depth of particular rock layers, the shape of underground formations, and the location and angle of faults. Seismic observation at the global scale can determine larger scale physical properties including the general structure and composition of the Earth's interior. The correct interpretation of seismic data depends on the accurate knowledge of the geology and material properties along the path of the seismic signal. Local variations in the material properties over a region are determined by analyzing the variations of the seismic signal with multiple source to receiver paths.

This thesis investigates the Cianten Caldera in Indonesia using data from a microseismic array for the adjacent Awibengkok geothermal power plant provided by the Chevron Corporation. This data is analyzed using Multiple Window Time Lapse Analysis (MWTLA)[6] to determine the proportion of energy of the direct arrival of the seismic signal lost due to either the scattering of the wave or the intrinsic absorption of the medium by measuring the scattering coefficient, g_o, and the seismic

albedo, B_o, across the Cianten Caldera. The scattering coefficient is a measure of how often a particular medium scatters a wave, changing its direction and amplitude. The seismic albedo is the ratio of the amount of energy lost due to scattering to the total amount of energy lost due to both scattering and intrinsic attenuation.[6] The scattered energy is recoverable since this energy is redirected rather than lost when the wave encounters a heterogeneity such as a change in density.[7] The energy from scattered waves reaches the seismometer, but the scattered waves will have followed longer paths than the direct arrival and will arrive later. The energy that is lost to absorption is not recoverable by the seismometer since the energy has been converted to heat as the wave moves through the medium.[7] These variables are related to geologic features by assuming that the largest coherent scatterers that a seismic wave encounters are fractures and that the absorption of energy happens most efficiently when the medium is free to move as in a liquid. Knowing the extent to which energy is absorbed or scattered implies the amount of fractures and liquid present in a certain area.

The distributions of fractures and fluids are very important to the operation of a commercial geothermal plant that relies on being able to extract enough hot water from the ground to supply its customers with electricity. This hot water is brought directly from the hot reservoir to the surface via a well, but the speed with which the liquid can seep into the well is controlled by the availability of pathways for the water to move from the pores within rocks of the reservoir to the well. A geothermal power plant extracts hot water to spin its turbines. The hot water is depressurized to create steam that spins a steam turbine. A generator converts this motion to electricity by inducing a current with magnets. A commercial geothermal plant that needs to supply a consistent amount of electricity must be able extract enough hot water at a steady rate to keep its turbines spinning constantly or it will be unable to meet the energy needs of its customers.

The Cianten Caldera is not suitable for commercial geothermal energy production unlike the the neighboring Awibengkok geothermal system also known as Salak.[23] The goal of this paper is to use MWTLA to examine the variations in the values

of the scattering coefficient and the seismic albedo within the Cianten Caldera and compare it with those found in the Awibengkok field. The variations in the scattering coefficient and the seismic albedo are then related to variations in the geology of the Cianten Caldera itself. The insight provided by this examination creates a better understanding of the geology of the Cianten Caldera and the manner in which the geology affects the physical properties of the Cianten Caldera. These results are used to investigate why the Cianten Caldera is not a commercial scale geothermal energy source.

These are important characteristics for a geothermal reservoir because of the way a geothermal energy system circulates water though the crust. The geothermal plant pumps cold water into the ground via one or more injection wells. That relatively cold water travels through pores and fractures in the hot rock deep underground. The now-hot water is then pumped to the surface via an extraction well. The geothermal power plant then uses a generator to convert the energy in the hot water to electricity. If the water is not hot enough, the heat will not efficiently be converted into electricity. If the porosity is not high enough, the geothermal plant will not be able to draw enough hot water out of the crust to create enough electricity to cover the cost of operation. When a reservoir contains hot rock and high porosity, a geothermal power plant is a sustainable and environmentally friendly source of electricity.

1.2 Organization

This thesis is broken into chapters in the following manner. Chapter 1 outlines the motivation and the organization of the paper before describing the geologic history of the Cianten Caldera and the surrounding region. Chapter 2 describes the synthetic two dimensional test case and two orthogonal planes from the microseismic data around the Cianten Caldera that were used in this paper. Chapter 3 describes Multiple Window Time Lapse Analysis (MWTLA), the method that was implemented to find the scattering coefficient and the seismic albedo for both datasets. Chapter 4 the results of the application of MWTLA to each of the two datasets. Chapter

5 discusses the possible implications of the results of MWTLA with respect to the geologic setting of the Cianten Caldera.

1.3 Geology

This paper specifically examines microseismic events located within and surrounding the Cianten Caldera. In order to show the geology that has shaped this area, the following three sections will examine the geology within and surrounding the Cianten Caldera on the scales of the tectonic region of the Sunda Arc subduction zone, the local area that includes the Awibengkok geothermal system, and the extent of the Cianten Caldera itself.

1.3.1 Regional Geology

The Cianten Caldera is directly to the west of the well-studied Awibengkok geothermal field, 60 km south of Jakarta, Indonesia on the island of Java as shown in Figure 1-1. Java is a part of the Sunda Arc, a 5,600 km chain of volcanic islands that lie between China and Australia. The Sunda Arc is on the edge of the Eurasian tectonic plate where the Eurasian plate meets the Australian plate. The collision of these two oceanic plates forms the subduction zone where the Australian plate is subducted underneath the Eurasian plate at the Sunda Trench. The Sunda Arc parallels the subduction zone from the superior Eurasian plate.

The volcanic islands of the Sunda Arc are a direct result of this subduction.[18] The process of subduction introduces water from the subducted plate to minerals in the upper mantle and deep crust which chemically lowers the melting point of those minerals until liquid melts form. In the case of a collision between two oceanic tectonic plates, these resulting melts rise to form underwater volcanoes that grow and eventually form islands given enough time.[8] This process forms volcanoes like those of the Sunda Arc, including those that make up the islands of Java and Sumatra.[18]

As a result of the volcanic origins of the Sunda Arc, the seamounts and islands of the Sunda Arc are composed of igneous rocks of various volcanic compositions

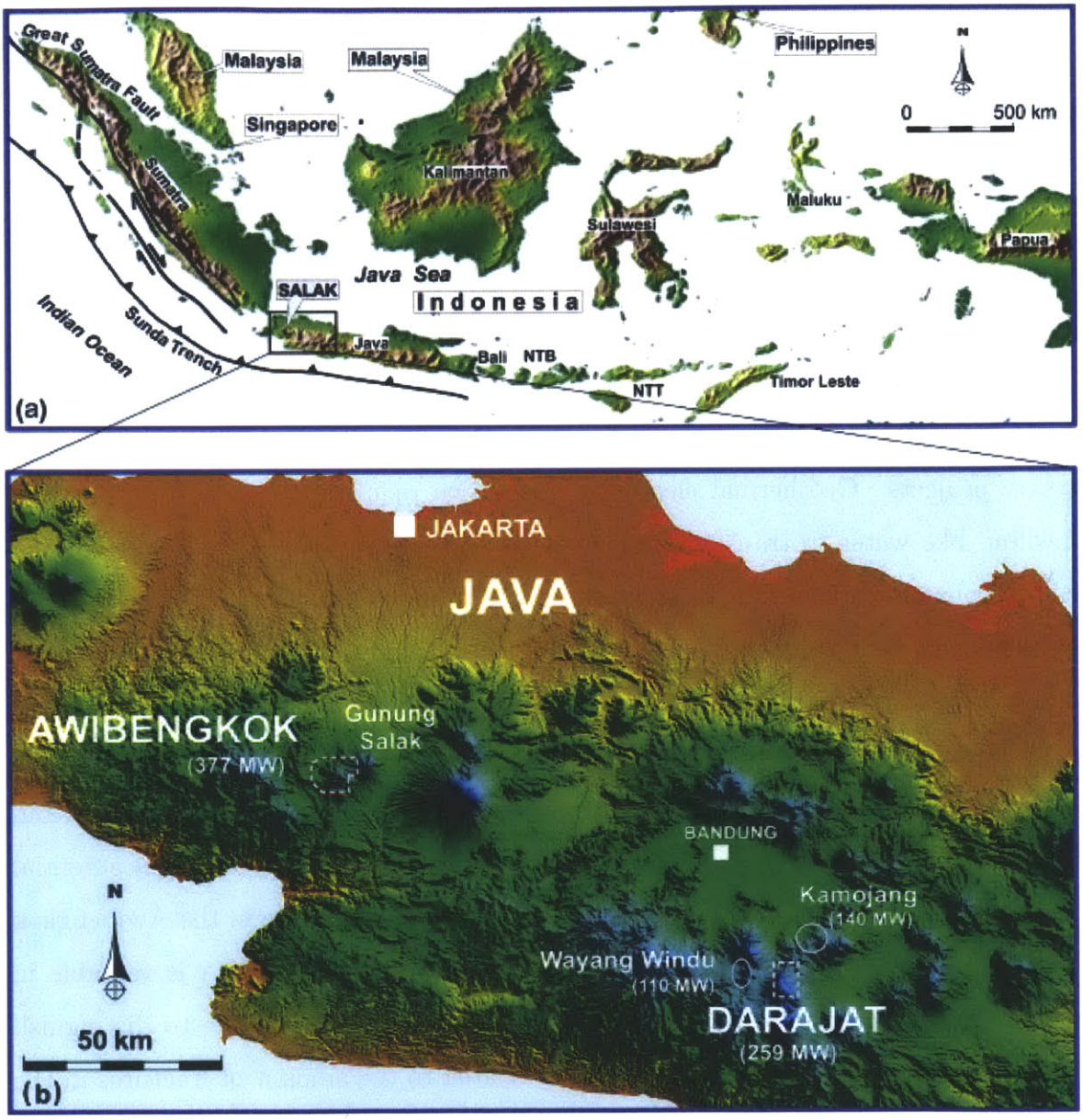

Figure 1-1: A map of Indonesia (Figure 1-1a) and western Java (Figure 1-1b). The extent of the contract for the Awibengkok geothermal field is shown by the dotted box on the left of Figure 1-1b. The Cianten Caldera is smaller than the Awibengkok field and lies immediately to the west of Awibengkok. This image was taken from Stimac et al., 2008.[23, p. 302]

and textures including basalts, andesites, rhyolites, and ash beds. The melts that formed these igneous rocks were derived from the melting of the mantle and Eurasian oceanic plate. The persistent volcanic activity that formed the Sunda Arc created many different types of volcanic structural features stacked on top of one another including volcanoes, calderas, dikes, sills, and plutons.[8]

The subduction zone to the south of Java is the source of the regional stress in western Java where the Cianten Caldera lies. The orientation of the convergence between the two plates at Java is approximately north-south at a rate of 6-7 cm/year. The maximum horizontal stress in western Java has been determined by evaluations of regional stress indicators and has been found to be approximately north-south.[23]

Volcanically active areas like the Sunda Arc are be well suited to geothermal electricity projects. Geothermal electricity generation requires a source of hot rock, a medium like water to transfer the heat between the reservoir and the surface, and enough porosity in the rock to allow the water to move through the reservoir on an economically viable timescale. The presence of magma in the crust in volcanically active areas increases the regional temperature gradient so that hot rock is accessible from less expensive, shallower wells. The pressures and fluctuations in temperature associated with tectonic and volcanic activity create joints, fractures, and faults within the rock units themselves and increase permeability. The porous rocks of a potential reservoir are likely saturated with water. These features combine in the Awibengkok geothermal field to make it a successful geothermal plant. MWTLA is valuable in examining the geology of potential geothermal fields since it is able to distinguish both the scattering coefficient, g_o, which is related to the amount of fractures in the seismic medium and the seismic albedo, B_o, that is related with g_o to the amount of liquids in the medium.

1.3.2 Local Geology

The proximity of the Cianten Caldera to the Awibengkok geothermal field as seen in Figure 1-2 means that the two areas contain many of the same rock units and have been affected by the same regional forces. However, the Cianten Caldera is not a com-

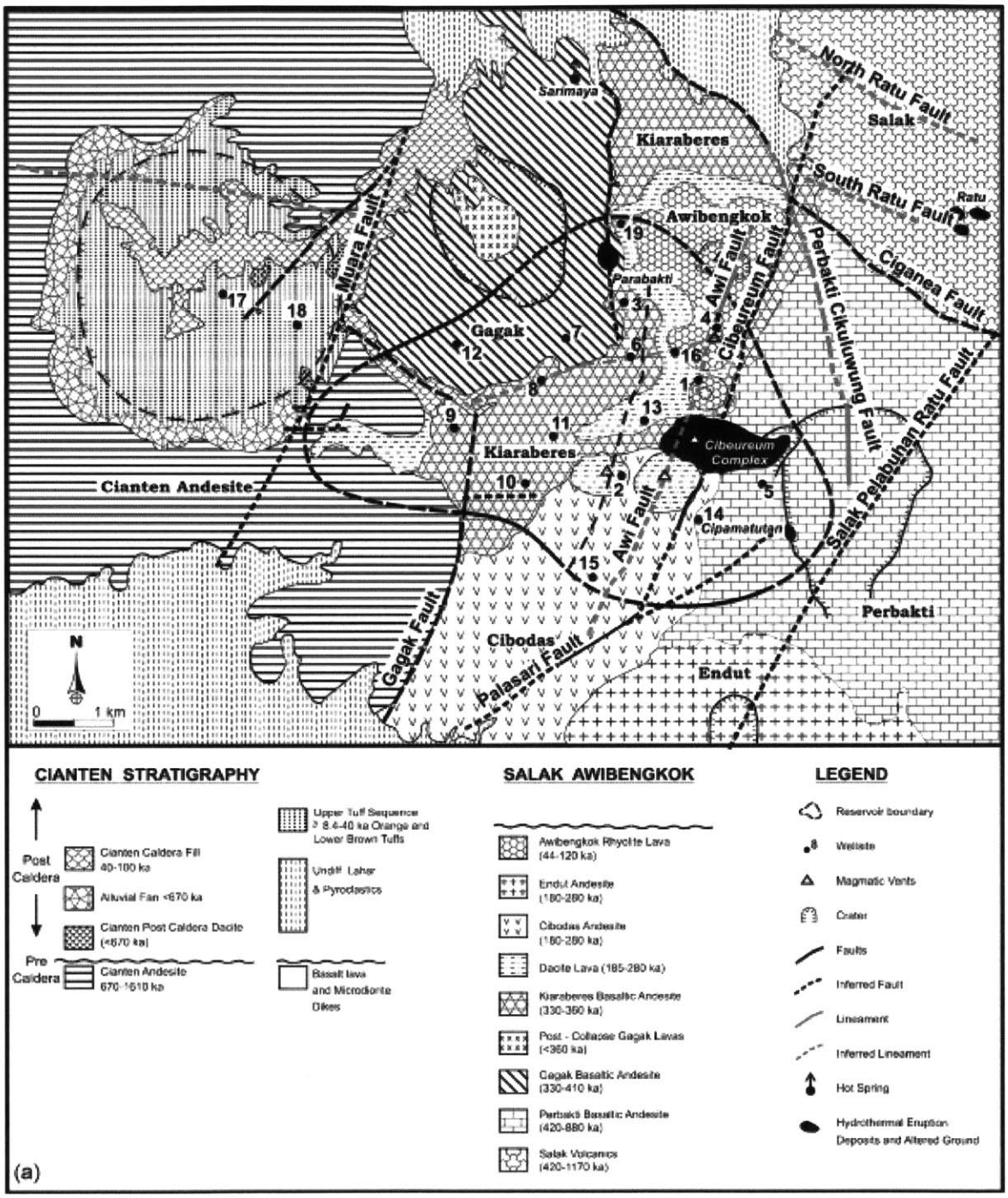

Figure 1-2: The geology of the Cianten Caldera and the Awibengkok geothermal field at the depth of the Rhyodacite Marker. The Cianten Caldera is the circular feature on the left. The productive Awibengkok field is the triangular outline in the central third of the figure. The Muara Fault hydrologically divides the two regions. The image was taken from Stimac et al., 2008.[23, p. 305]

mercially viable geothermal energy source. Awibengkok produces 377 MWe of electricity for the region from approximately 18 km^2 of proven geothermal reservoir.[23] The Awibengkok field is geothermally productive because the temperature of the rock in the reservoir ranges from 235°C to 310°C and the reservoir is naturally fractured and saturated with water.[1] The field has been hydrofraced to increase the porosity.[29] This temperature, porosity, and water content has allowed the Awibengkok field to reliably produce electricity since 1994.[23] The Cianten Caldera is separated from the Awibengkok field by the Maura Fault. The Cianten Caldera has a lower temperature which has caused many of the fractures in the Cianten Caldera to be sealed by mineral precipitation. The Cianten Caldera and the Awibengkok geothermal field have very different properties despite the fact that they are adjacent to one another.

The stratigraphy of Awibengkok is shown in Figure 1-3. The oldest units at the bottom of the stratigraphic column are marine sedimentary rocks that were formed prior to volcanic activity when the oceanic floor was gradually collecting sediment. These compacted sediments have less porosity, permeability, and hydrothermal alteration than the volcanic sequences above them. The units above these sediments are igneous layers of andesitic and dacitic composition. The alternating composition formed as the melt evolved over time due to crystal fractionation, crustal assimilation, or magma mixing. Most of the Awibengkok reservoir is contained within the lower andesite volcanic layer.[23] The reservoir has an impermeable smectite clay cap called the Rhyodacite Marker that prevents water even under pressure from rising through the stratigraphic column. This smectite clay cap of the geothermal reservoir is a common feature in volcanic geothermal fields that is formed by hydrothermal alteration of the existing rocks at high temperatures.[23] Volcanic activity in the Awibengkok area has created multiple intrusions that have disturbed the stratigraphic column. These molten bodies thermally alter the layers they come into contact with, forming contact aureoles.[1] These intrusions are the source of the heat that the Awibengkok geothermal power plant uses to produce electricity. These intrusions also heat fluids which rise until they are trapped at the smectite cap in the Awibengkok reservior.[23]

Without the cap, the fluids would be free to rise towards the surface and dissipate the heat they contain. The cap forces these fluids to pool underground where they are insulated and able to be retrieved by wells. As a result, the reservoir is can be a profitable geothermal energy source.

The geology and structure of the Cianten Caldera and the Awibengkok field at the Rhyodacite Marker is shown in Figure 1-2. The multiple faults in the Awibengkok region generally trend in the north-northeast direction. Some of these north-northeast faults that cut the Awibengkok geothermal field, including the Gagak Fault and the Cibeureum Fault, are semi-permeable and have segmented the field into four geochemically semi-independent cells. The Muara Fault is an impermeable fault, and it geothermically isolates the Cianten Caldera from the Awibengkok field.[23] The surface geologic map of the Awibengkok area is shown in Figure 1-4 and has similar features. Figure 1-4 contains the full extent of both the active Awibengkok field to the east and the Cianten Caldera on the west. This image is also shown in Figure 2-4 with the locations of the sources and receivers from the microseismic survey used for analysis. The geology of the area is difficult to determine due to thick tropical vegetation and sediments so there is some uncertainty in some of the details including the extent of the Maura Fault.[23]

1.3.3 Cianten Caldera

A caldera is formed when a volcano collapses under its own weight after an eruption empties the magma chamber underneath the volcano.[8] The Cianten Caldera is a small caldera with a diameter of 4.5 km and an area of 16 km^2 that erupted approximately 16 km^3 dense rock equivalent (DRE) of material prior to its collapse between 150,000 and 670,000 years ago.[24] The Cianten Caldera is outlined in Figure 1-2 by the circular ring fault created during this collapse. Most of the exposed surface of the Cianten Caldera visible in this figure is part of the Upper Rhyolite unit or the alluvium.[23]

Figure 1-5 shows a facies model of the Cianten Caldera taken from Stimac et al., 2008. This model is based on the limited outcrop available in the Cianten Caldera,

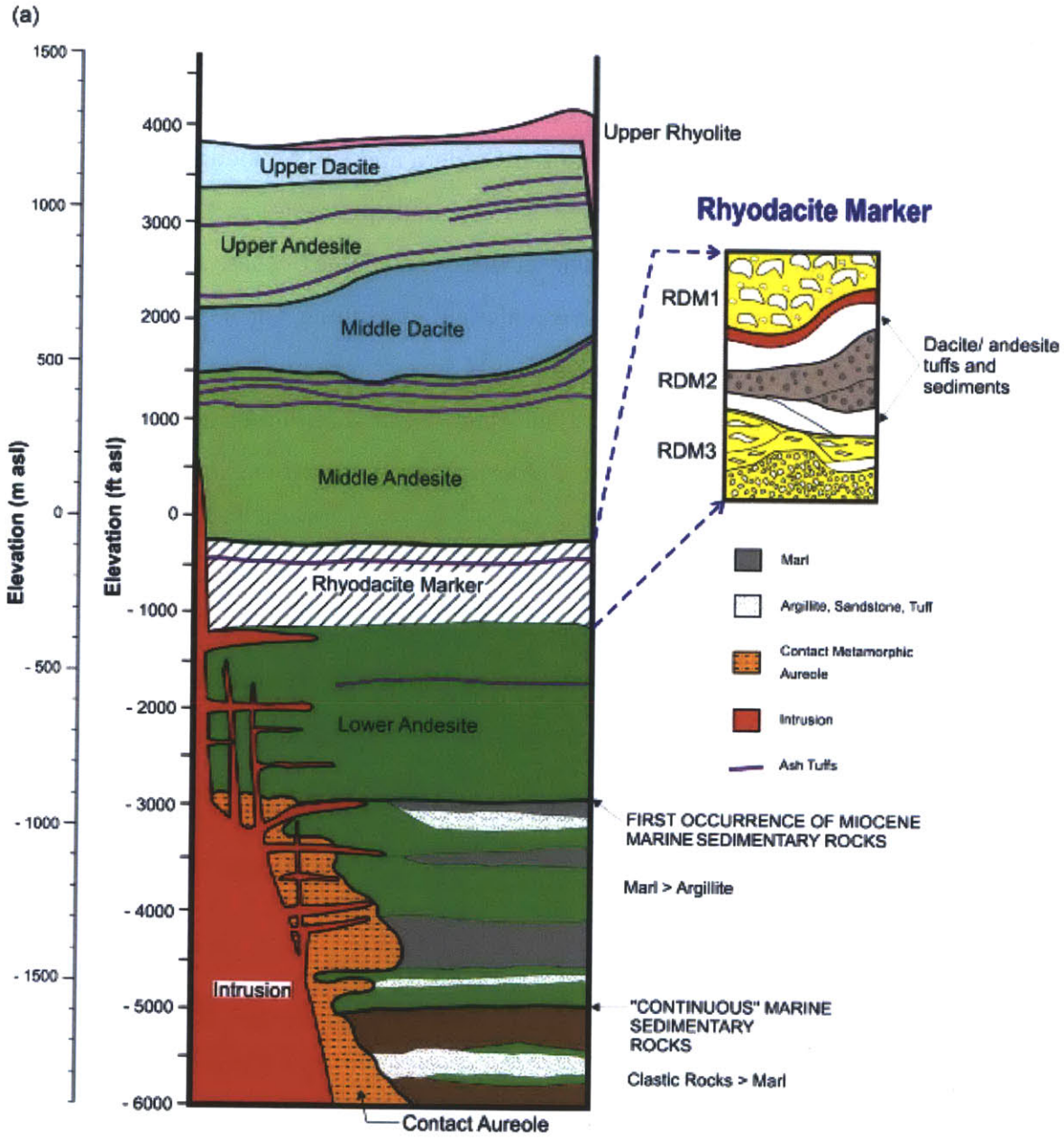

Figure 1-3: A stratigraphic column of the Awibengkok geothermal field. The oldest, deepest rock units are marine sediments. Above these sediments are alternating layers of andesitic, dacitic, and rhyolitic volcanic material. The layered stratigraphy is interrupted by younger intrusions that have thermally altered the rock surrounding the intrusion. The Awibengkok geothermal reservior is in the Lower Andesite and is capped by a smectite clay layer at the Rhyodacite Marker. This figure was taken from Stimac et al., 2008.[23, p. 310]

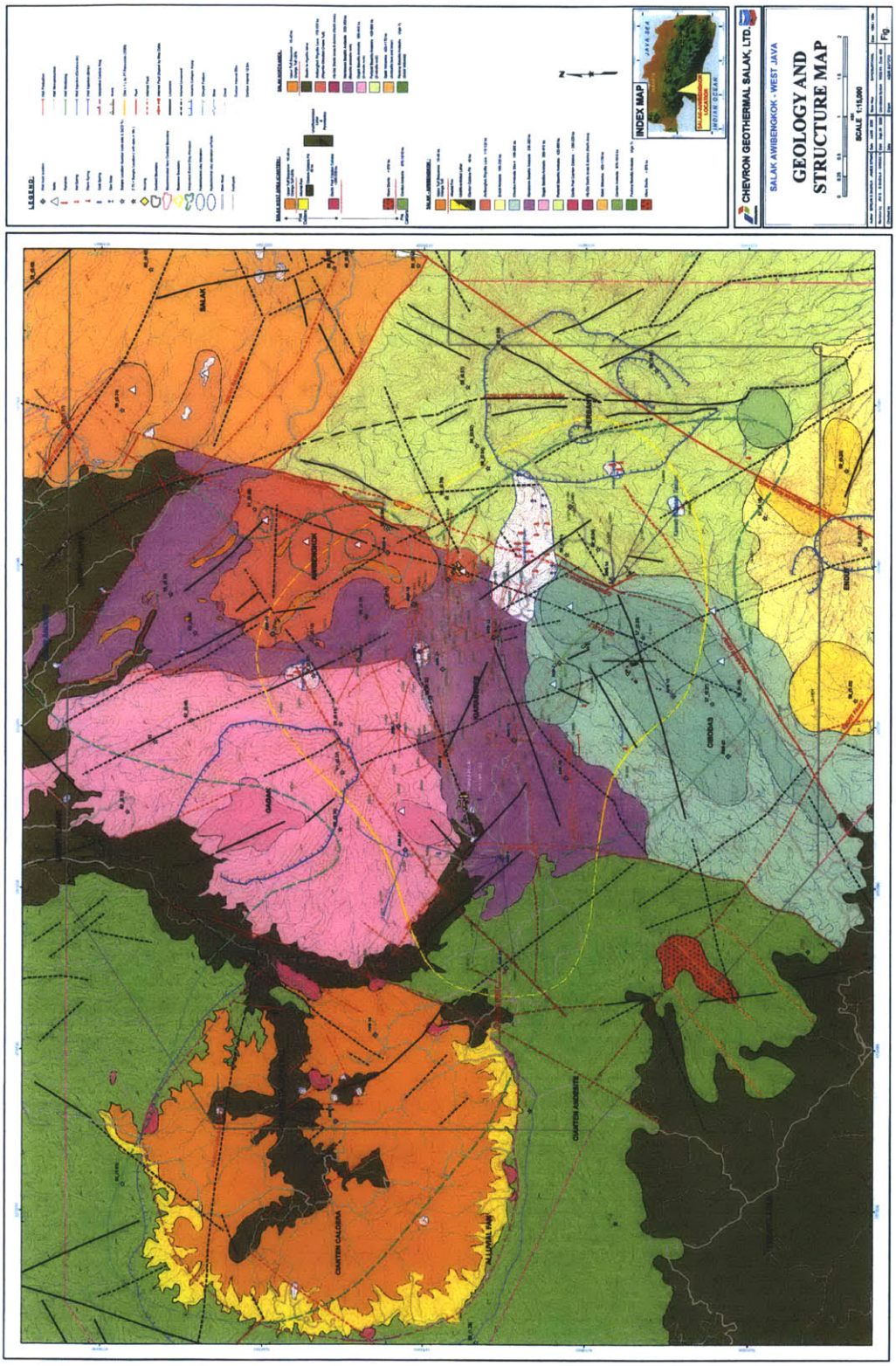

Figure 1-4: A geologic map of the Awibengkok region. The Cianten Caldera is the orange circular structure on the west side of the map. The productive Awibengkok field is the triangular shape. The Maura Fault is an impermeable fault that divides the two areas. This map was made by Stimac et al., 2009.[25]

local stratigraphy, and the structure of other small calderas.[24] The original extent of the volcano that formed the Cianten Caldrea and the original, uneroded shape of the caldera is visible in Figure 1-5.

The oldest rocks in this model are the basement of Miocence sedimentary rocks that were in place prior to volcanic activity. Much of these sediments have been altered after their deposition through contact metamorphism. The unit above these sediments is composed of the volcanic rock that was erupted before the collapse that formed the caldera. The unit of megabreccia and the caldera ash-flow tuff is from after the caldera collapse. The top of this layer became the floor of the caldera after the collapse. A lake formed in the caldera and collected the lacustrine deposits. The fan and talus deposits also eroded into the lake. Eventually, the lake that filled the caldera breeched the rim of the caldera and drained. The Cianten Caldera then began to fill with debris and ejecta from other eruptions until the present day.[23]

The Cianten Caldera has been affected by both pre-caldera and post-caldera volcanism. There are many intrusions of different ages embedded in different layers of the caldera. These intrusions thermally altered the rock they contacted. Most of these intrusions predate the collapse of the caldera as small calderas rarely have significant post-caldera volcanism. The last of these intrusions was likely a post-caldera dome formed from the residual magma shortly after its collapse.[24]

Interest in the Cianten Caldera began when geophysical surveys at the borders of the active Awibengkok field found the presence of a low resistivity layer in the Cianten Caldera that could have been an extension of the low resistivity, anisotropic, smectite clay layer that caps the active Awibengkok geothermal reservoir. Prior to drilling, it was believed that the smectite clay layer could have originated from the sediments in the lake that formed after the creation of the caldera.[23] A local high gravity anomaly on the southeastern rim of the caldera was thought to indicate the presence of shallower basement or an intrusion.[23]

After wells were drilled in the Cianten Caldera, it was found to not be suitable for an expansion of the Awibengkok goethermal field. The Cianten Calera has subcommercial temperatures, numerous intrusions, and a shallow basement.[23] The low

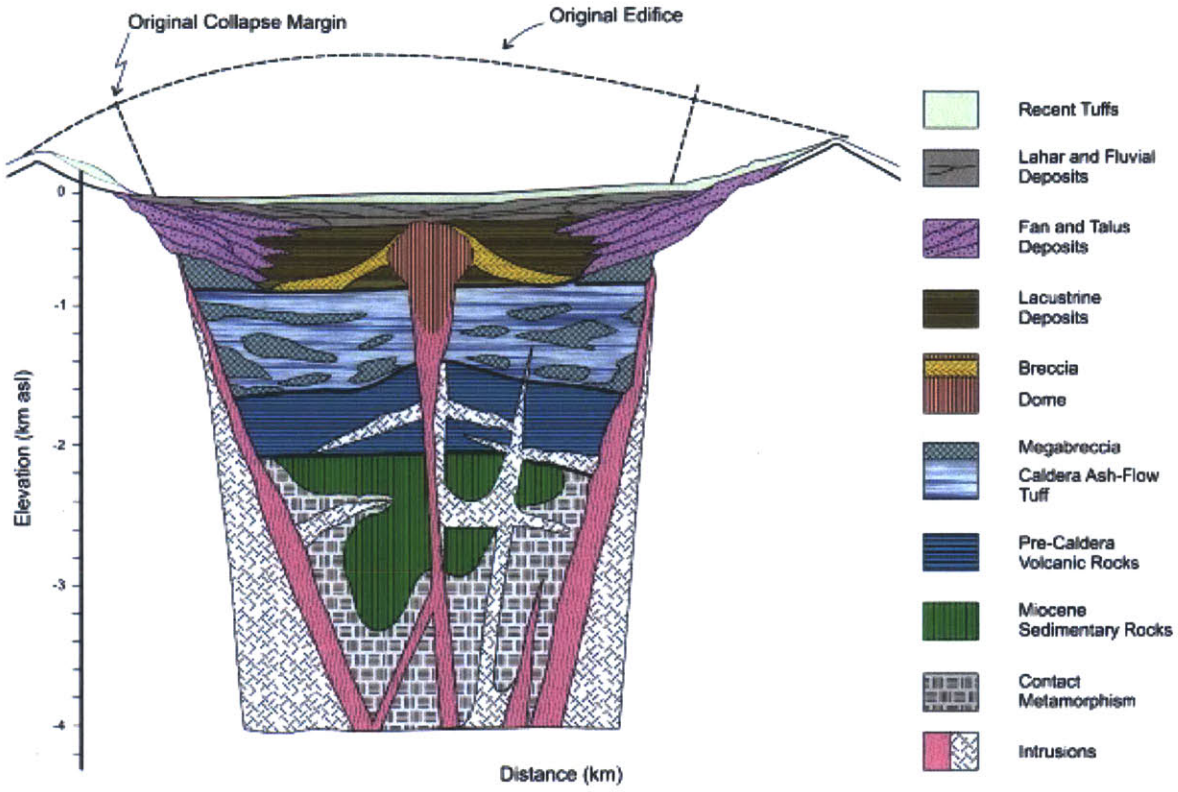

Figure 1-5: A facies model of the Cianten Caldera based on outcrop, local stratigraphy, and the structure of other calderas of a similar size and tectonic setting. It contains a basement of marine Miocene sedimentary rocks overlain by pre-caldera volcanic rock. Above these rocks are post-caldera megabreccia and a caldera ash-flow tuff. The caldera's lacustrine deposits and the eroded fan and talus deposits filled in much of the caldera basin. Other deposits and recent tuffs fill the top of the section. Pre-caldera and post-caldera intrusions have cut and metamorphosed the layers they contacted. This image was taken from Stimac et al., 2008.[23, p. 327]

resistivity layer in the Cianten Caldera was later confirmed to be a smectite clay layer by rock cuttings obtained from drilling through this layer.[23] The smectite clay layer is an anisotropic feature which affects seismic data. However, drilling also showed that subsurface temperatures in the Cianten Caldera are much lower than in the Awibengkok field and not of commercial value.[29]

The Cianten Caldera was thought to have the potential to be a commercial geothermal field like the Awibengkok field immediately adjacent to it. However, the temperatures in the Cianten Caldera are too low for this to be possible. The knowledge gained by finding the distribution of the scattering coefficient and the seismic albedo over the Cianten Caldera and across the Maura Fault from the application of MWTLA to microseismic data should shed light on the interior structure of the Cianten Caldera. A better understanding of the interior geology of the Cianten Caldera would help explain the reasons why the Cianten Caldera has lower temperatures and sealed fractures due to mineral precipitation that make the Cianten Caldera not expected to be as geothermally productive as the adjacent Awibengkok geothermal field.

The geology of the Cianten Caldera gave it the potential to be a good geothermal candidate. Other calderas have been successful geothermal energy producers including the Long Valley Caldera in California.[21] This caldera has been well studied because it is seismically active and there was concern that it would become an active volcano once more.[9] Seismic waveforms from this area have been processed with MWTLA in order to find values for the scattering coefficient and the seismic albedo. The results of this study are discussed in Section 3.3.

Hawaii is another volcanic area that has been considered for geothermal energy production. The geology in the area has features that are similar to those of the Awibengkok field that would make electricity generation possible including fractured volcanic rock and a high geothermal gradient. The region has a high temperature gradient due to the intrusions that are in the crust.[13] The results of the application of MWTLA to this area is discussed in Section 3.3.

Chapter 2

Data

This chapter describes both the two dimensional synthetic acoustic dataset that was created to test the MWTLA code and the Awibengkok microseismic dataset from the Awibengkok geothermal field that are analyzed in this paper.

2.1 Synthetic Acoustic Data

A synthetic two dimensional, acoustic dataset was created in order to test the MWTLA code before adding the complications of field data. The setup of the receivers for the dataset can be seen in Figure 2-1. Each line of receivers contains 1024 receivers, and each receiver has a seismic trace for each of the 9 sources. Synthetic traces were created for three different cases by using moving the source locations to one quarter of the full depth, one half of the full depth, and three quarters of the full depth. Synthetic traces were created for three different velocity models that were generated by adding zero mean Gaussian random noise with a correlation length of 0.05 km to a background velocity of 3 km/s. To simulate intrinsic attenuation, an artificial exponential decay was applied to all of the traces of e^{-ar} where a is a constant value of 0.3 and r is the distance between the source and the receiver. Examples of the traces that were used for the analysis of the acoustic case can be seen in Figure 2-2.

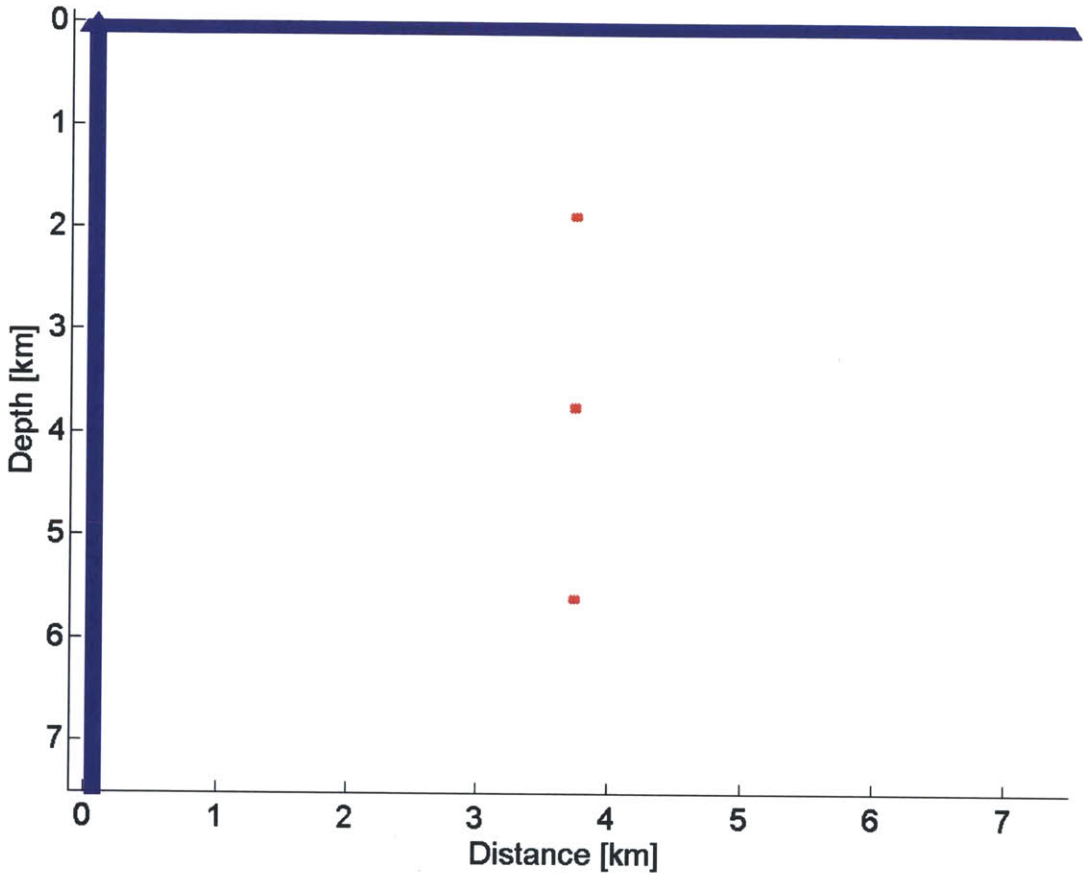

Figure 2-1: This figure shows the general distribution of the sources, shown in blue, and receivers, shown in red, for the synthetic acoustic dataset. There are two orthogonal lines of 1024 receivers and nine sources in a three by three matrix.

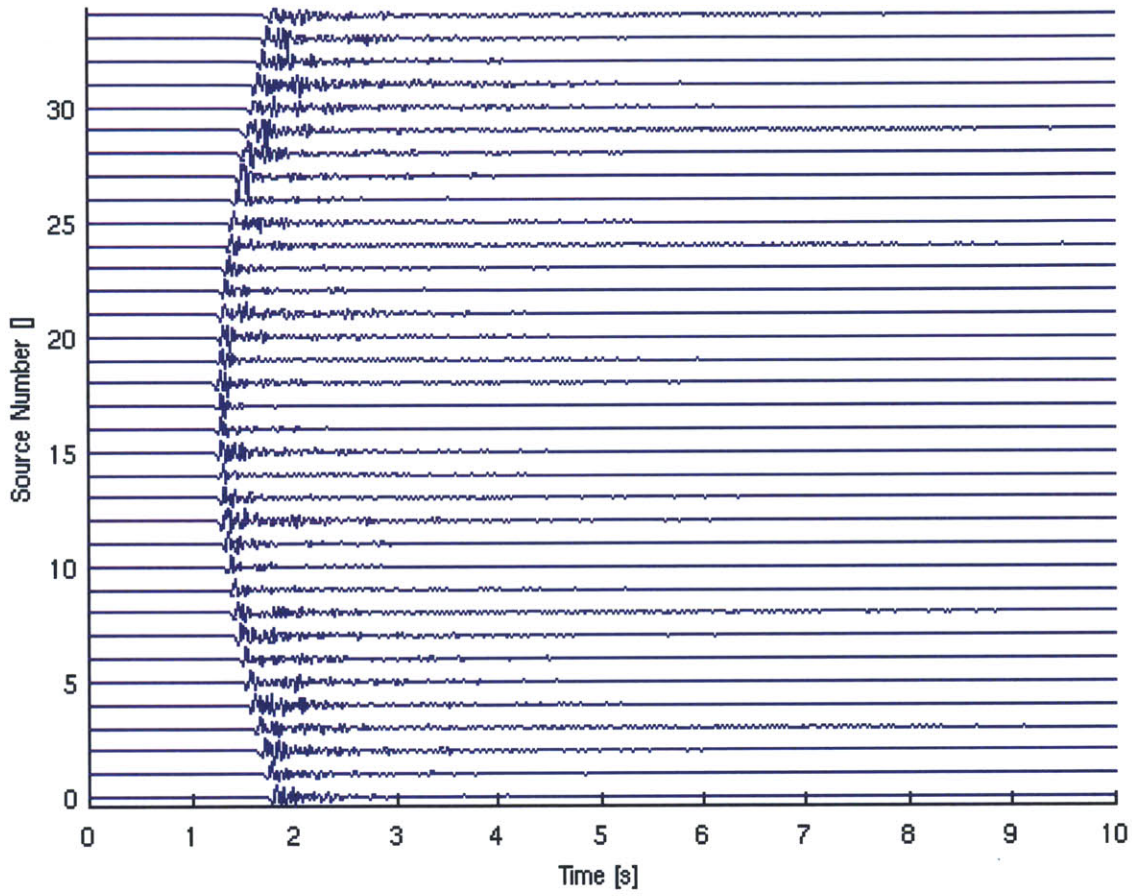

Figure 2-2: This figure shows the full length of selected traces from surface line of receivers for source 1. The traces have been normalized by their maximum value.

2.2 Microseismic Data

The microseismic dataset that is used in this thesis has been generously provided by the Chevron Corporation. The data is from an array of three component receivers within and surrounding the active Awibengkok geothermal field. This array monitors microseismic activity from injections and hydrofracing new wells. The full dataset was recorded from 2005 to 2010. The magnitudes of the recorded sources range from -0.6 to 3.6. The vast majority of events recorded have a magnitude between -.02 and 1.5. More smaller events likely took place, but they were not recorded or could not be separated from the random background noise. Relatively larger events like the 3.6 magnitude event did occur and were recorded. These larger events happen much less frequently than the smaller events. Larger events require exponentially more accumulated stress than smaller events and this larger amount of stress requires a longer period of time to accumulate.

A subset of the full dataset was selected to analyze in this paper based on the distribution of receivers and the activity in the Cianten Caldera. Some receivers were moved as different parts of the active geothermal field were being explored, hydrofraced or injected.[29] This was the case when Chevron investigated the Cianten Caldera by the drilling of the Awi-18 well. One month in particular, October 2008, was selected for further examination based on the number and quality of events around the Cianten Caldera. Each of the waveforms that were recorded over this period were visually inspected for clipping, a good signal to noise ratio, and the ability to distinguish the P-wave and S-wave arrival times.

The locations of the full set of earthquakes whose waveforms passed the quality control process can be seen in Figure 2-3. The position of the data relative to the geology of the region can be seen in Figure 2-4. This figure shows the geologic map, all of the receivers in the selected data, and the sources that fell within the bounds of the geologic map.

These images show a prominent planar west to east trend in the sources including two of the receivers. Another south to north line that passes through the Cianten

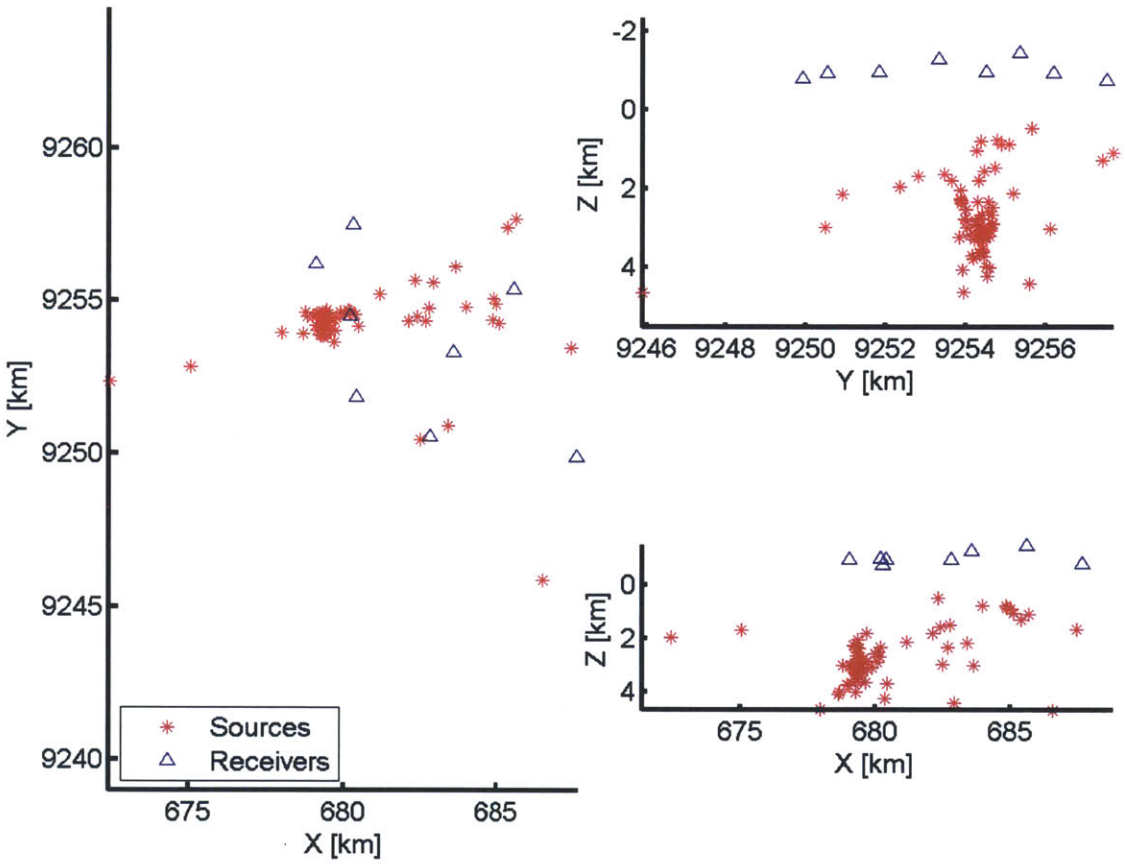

Figure 2-3: This figure shows the distribution of all of the sources and receivers from October 2008 that passed the quality control measures.

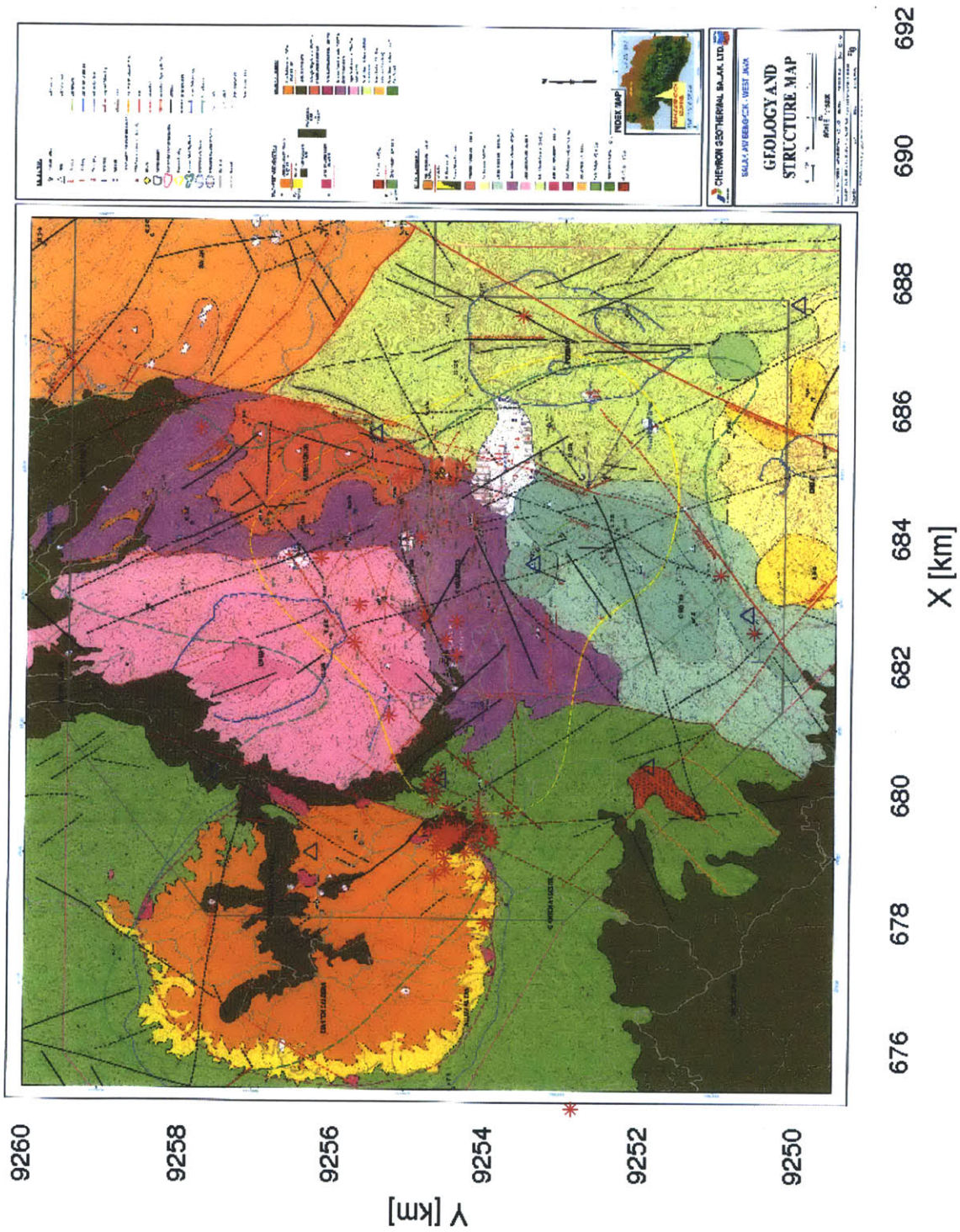

Figure 2-4: This figure shows the distribution of the sources and receivers on the geologic map. There are a number of sources on both sides of the Maura fault which separates the Cianten Caldera from the active Awibengkok geothermal field. One receiver is located within the Cianten Caldera.

Caldera can be constructed using four receivers and a number of sources. We use these two different planar trends for the two dimensional analysis made later in the paper. The selected data for the west to east plane are shown in Figure 2-5. The selected data for the south to north plane are shown in Figure 2-6. Figure 2-7 shows both of these planes of data from a map view including the overlapping sources and receiver common to both datasets. Due to uncertainty in the origin times and the S-wave arrival times, the error in the location of the events range from tens to hundreds of meters.[17]

Figure 2-8 is an example of normalized seismic traces from the subset of data that were used in this paper. These traces are from the north component of receiver 8 for the sources from the west to east plane of data. This figures shows the first 15 seconds of the 30 seconds long traces. Many of the traces do not have data for the full 30 seconds as the receiver stopped recording when the signal to noise ratio became too small. The magnitude for the segment of traces that is beyond the recorded data from the receiver is set to zero.

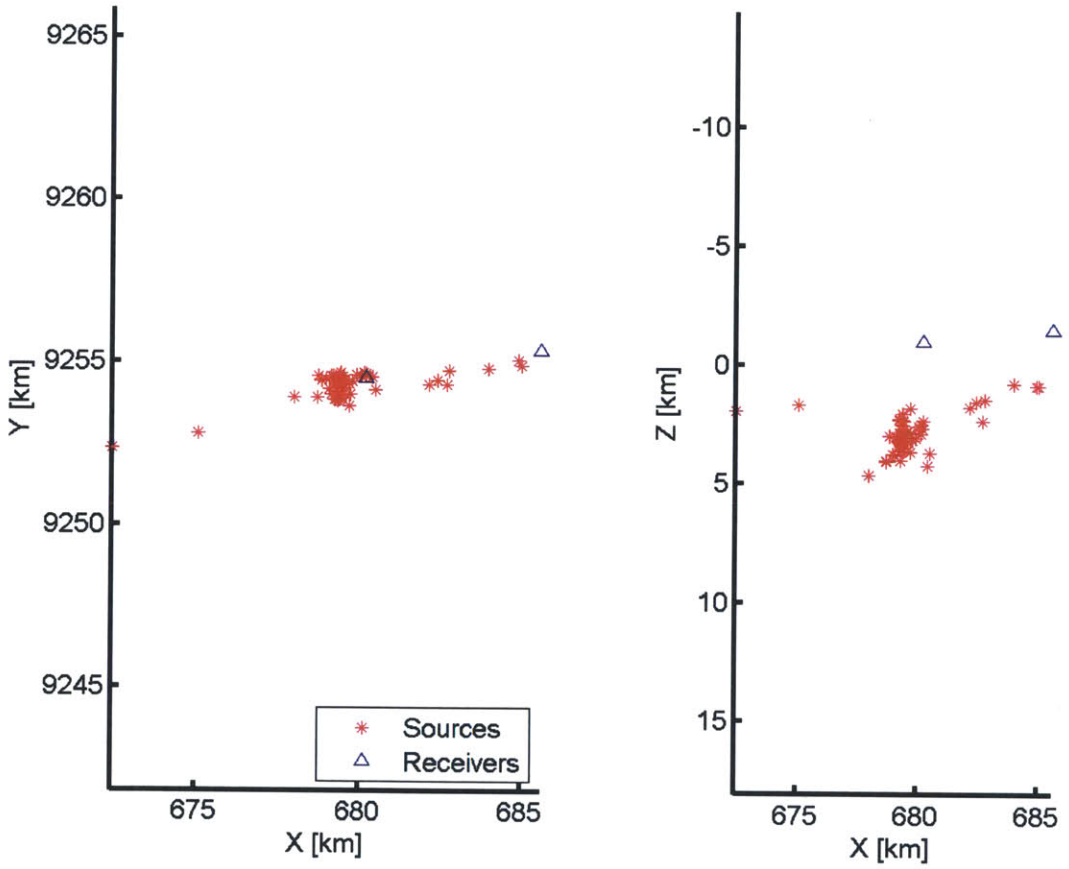

Figure 2-5: This figure shows the selected plane of sources and receivers that runs west to east across the Cianten Caldera and the Awibengkok field.

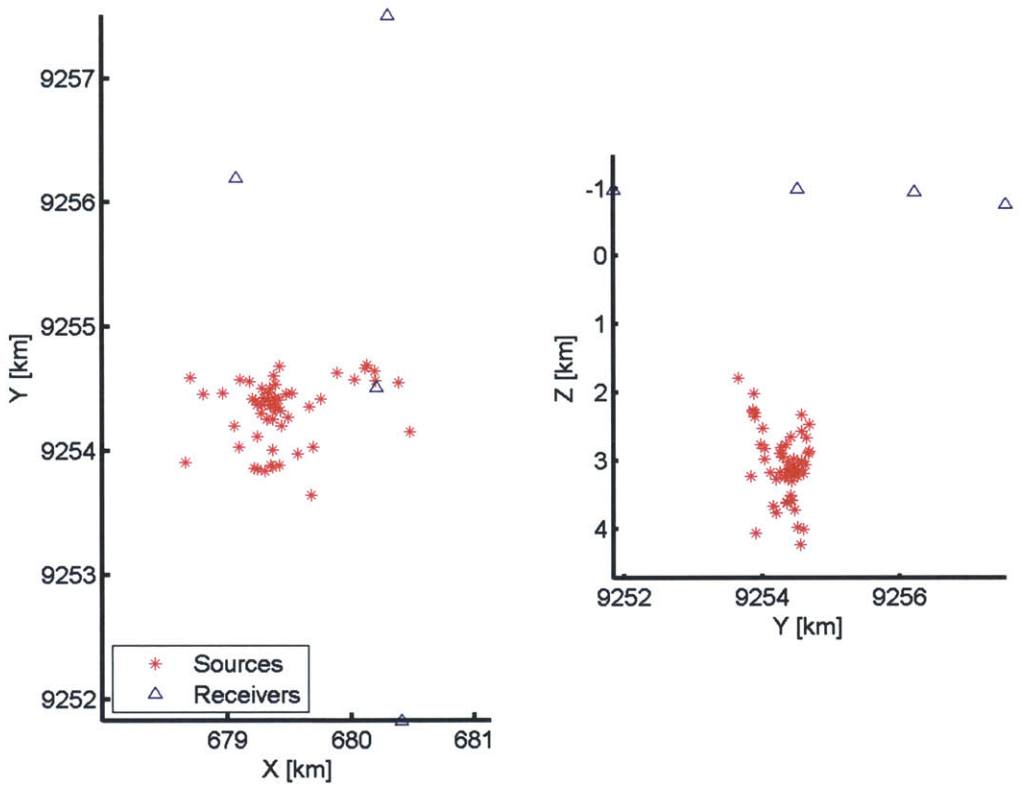

Figure 2-6: This figure shows the selected plane of sources and receivers that runs south to north across the Cianten Caldera.

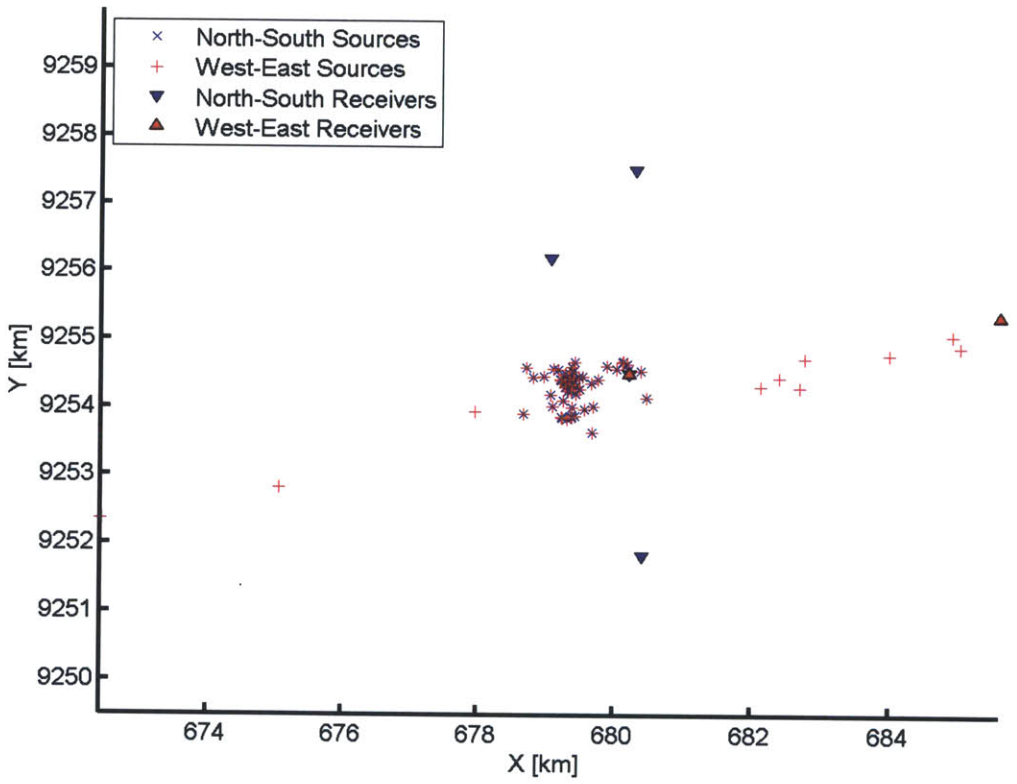

Figure 2-7: This figure shows both the west to east and south to north planes of sources and receivers.

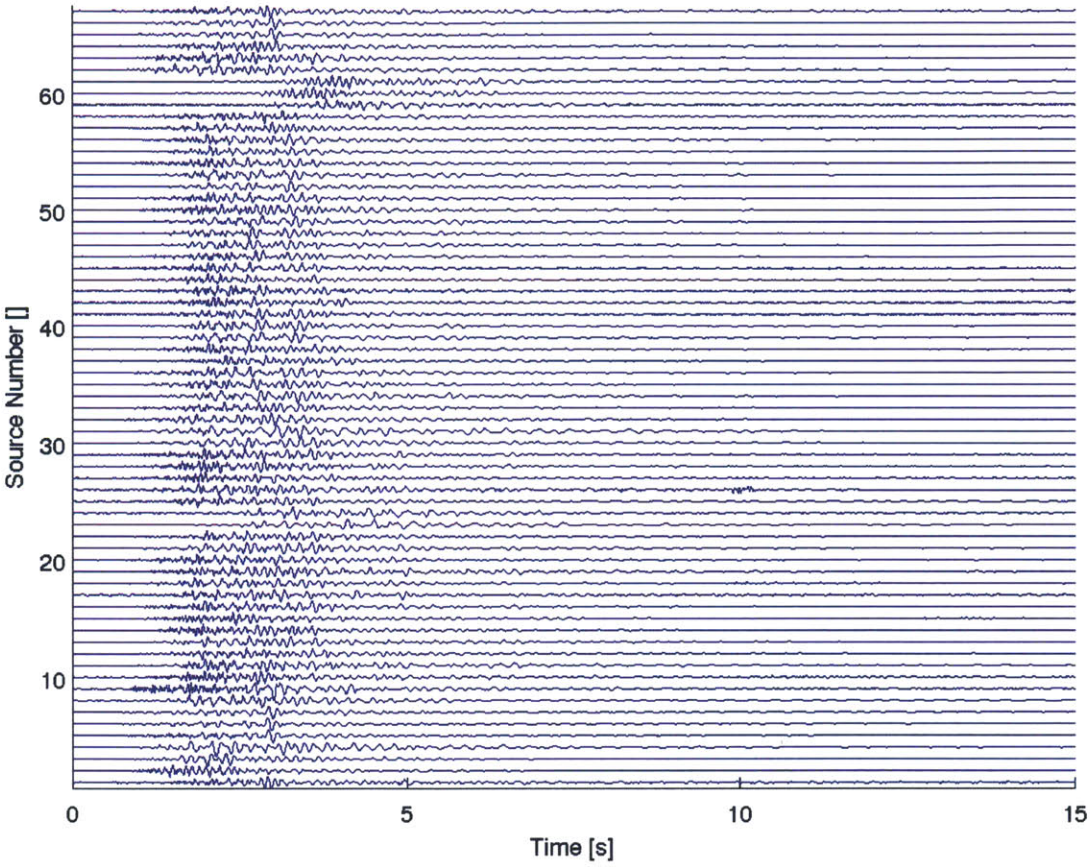

Figure 2-8: This figure shows the first 15 seconds of the normalized traces from the north component of receiver 8 for the sources from the west to east plane of sources. The full traces are 30 seconds long, but a shorter section is shown here for detail.

Chapter 3

Method

This chapter details the theory behind the Multiple Window Time Lapse Analysis (MWTLA) method developed by Fehler et. al. in their 1992 paper. Then this chapter describes MWTLA and the process by which MWTLA is used to determine the scattering coefficient, g_o, and the seismic albedo, B_o, from the seismic traces.

3.1 Theory

The direct arrival energy for a seismic signal decays faster than simple geometric spreading can account for. This attenuation occurs either from waves scattering off of heterogeneities in the medium or from intrinsic absorption of energy as heat because of anelastic behavior in the medium. Scattering does not result in a loss of energy as scattering simply causes a change in direction or a phase shift of a wave. Intrinsic absorption does result in the wave losing energy when seismic energy is converted into heat.[11]

The process of scattering requires that the scattered wave covers a greater distance than the direct wave, so the scattered wave will arrive after the direct wave. Consequently, the portion of the seismic trace that is immediately after the arrival time will be dominated by the direct wave, and the coda of the seismic trace will be dominated by the scattered waves. This property that separates the intrinsic attenuation of a wave from the scattering of a wave is the basis of MWTLA.

A direct result of the fact that the direct arrival is dominated by intrinsic attenuation and the coda is dominated by scattering is that the relationship between the amount of energy in the direct arrival and the amount of energy in the coda is related to that amount of intrinsic absorption and scattering. MWTLA measures two different ratios to compare the amount of energy in the seismic traces. These ratios use the measurements of the energy in the wave immediately after the S-wave arrival and in the coda of the wave. The first ratio, R_1, compares the amount of energy in the first part of the wave to the amount of energy in the coda. In the case there is a lot of scattering, R_1 will be smaller since the coda will contain more energy. The second ratio, R_2, compares the amount of energy in the first part of the wave at one distance to the amount of energy in the first part of the wave at a larger distance. In the case that there is a large amount of intrinsic attenuation, R_2 will be larger since there will be less energy in the more distant wave. Similarly, in the case that there is a large amount of scattering attenuation, R_2 will also be larger since there will be less energy in the more distant wave. The effects from scattering and intrinsic attenuation, together known as total attenuation, cannot be distinguished from one another by this ratio alone.

The scattering coefficient, g_o, is a measurement of how much a medium scatters an incident wave. The scattering coefficient is defined as

$$g_o = \frac{1}{l}, \tag{3.1}$$

where l is the mean free path measured in kilometers. The mean free path is the average distance the wave can travel between scattering events.[26] The mean free path is dependent on the frequency of the wave, because seismic waves are most efficiently scattered by heterogeneities that are approximately the size of a wavelength. Consequently, the frequency of the wave determines the size of the heterogeneities from which the wave can reflect and waves with different frequencies will scatter from different objects with different mean free paths.[7]

The scattering quality factor, Q_s, is related to the scattering coefficient, g_o, by

$$Q_s = \frac{\omega}{g_o V} \tag{3.2}$$

and the intrinsic quality factor, Q_i, is similarly related to the intrinsic absorption coefficient, α, by

$$Q_i = \frac{\omega}{\alpha V}, \tag{3.3}$$

where ω is the frequency of the wave, and V is the seismic velocity of the wave in the medium.[6]

The seismic albedo, B_o, is defined by

$$B_o = \frac{Q_s^{-1}}{Q_s^{-1} + Q_i^{-1}} = \frac{g}{g + \alpha}, \tag{3.4}$$

where Q_s is the scattering quality factor and Q_i is the intrinsic quality factor.[6] The inverse of the scattering quality factor and the inverse of the intrinsic attenuation quality factor describe the amount of attenuation due to scattering and intrinsic absorption respectively. B_o ranges in values from 0 to 1. When B_o approaches 0, g approaches 0 km^{-1} and l, the mean free path of the wave, approaches infinity. The intrinsic attenuation of this wave is undetermined. When g_o is much larger than 1 km^{-1}, there is effectively no traveling wave as the medium dissipates the energy in the wave almost immediately by converting it to heat or other forms of intrinsic absorption. When $B_o = 1$, the medium exhibits perfect scattering with no losses due to dissipation of the energy of the wave as heat.[26] Most materials within the Earth fall somewhere between these two extreme cases. When $B_o < 0.5$, intrinsic attenuation is the dominant mechanism, and when $B_o > 0.5$, scattering is the dominant mechanism.[27]

The total attenuation, Q_t, is

$$Q_t^{-1} = Q_i^{-1} + Q_s^{-1} \tag{3.5}$$

since the only two ways for the direct wave to lose energy are intrinsic attenuation and scattering.

The scattering coefficient, g_o, and the intrinsic attenuation coefficient, α, are both determine by the geology of the region. When there are more heterogeneities on the scale of the wavelength of the wave and when these heterogeneities are closer together, the scattering coefficient will increase. These heterogeneities could be fractures or changes in the density or other properties of the medium the wave travels through. Similarly, the intrinsic attenuation coefficient is related to how well the medium is able to dissipate heat. Softer medium or the presence of water in the pores of the rock will increase the amount of energy that is lost as heat as the wave passes through it. The goal of this study is to relate these coefficients to the geology of the Cianten Caldera and the surrounding area.

When scattering is the dominant attenuation mechanism, the region contains more heterogeneities on the scale of the wavelength of the seismic wave such as fractures or changes in composition. When intrinsic attenuation is the dominant attenuation mechanism, the regions contains more attenuating features such as a higher water content or softer rock that is better able to convert seismic energy to heat. Both high values for scattering and attenuation are good for a geothermal reservoir. A high scattering coefficient, especially in an area that is more homogeneous than a volcano, could indicate large amounts of fractures that could be high permeability pathways to move water through the reservoir and into the well on a timescale that enables a geothermal plant to operate. A high attenuation coefficient could indicate that the region is saturated with a large amount of water, potentially indicating a larger porosity that would mean there is more water for the geothermal plant to use. A larger porosity could also indicate a larger permeability.

3.2 Multiple Window Time Lapse Analysis

MWTLA is based on the radiative transfer theory. The first methods that addressed the manner in which waves scatter were simple and included single scattering for

weakly scattering areas and diffusion for strongly scattering areas. Then the multiple scattering model allowed the calculation of scattering for a finite number of scatterers.[6] The radiative transfer theory is a method used to calculate the response of the intensity of a signal to passing through a medium that has an indefinite number of scatterers. In this application, we assume that scatterers are isotropic scatterers arranged uniformly throughout the medium and that only body waves are recorded.[26]

The raw seismic traces should be corrected for source and site amplification factors as well as geometric spreading prior to applying MWTLA.[6] The corrected seismic traces can be used to calculate two values, R_1 and R_2, directly from the seismic traces by using the ratio of energy at different portions of a seismic wave.

As explained in Section 3.1, the portion of the seismic trace immediately after the arrival time is dominated by the direct wave and the coda is dominated by the scattered waves. Time windows measured from the S-wave arrival time are used to specify these two distinct portions of a wave. The first time window contains the direct arrival that has not been overly scattered. The third time window contains the coda which has been scattered many times. The second time window lies between the first time window and the third time window and is unused. For this analysis, the first time window is from 0 to 5 seconds from the S-wave arrival and the third time window is from 10 to 26 seconds from the S-wave arrival. The coda is limited to 26 seconds because of the duration of the waveform recordings.

R_1 is defined as

$$R_1 = log_{10}\left(\frac{E_{1a}(r_a)}{E_{3a}(r_a)}\right) \tag{3.6}$$

and R_2 is defined as

$$R_2 = log_{10}\left(\frac{r_a E_{1a}(r_a)}{r_b E_{1b}(r_b)}\right) \tag{3.7}$$

where E_1 is the energy that arrives during the first time window, E_2 is the energy that arrives during the third time window, r is the distance between the source and the receiver, and the subscripts a and b denote a near source and a far source,

respectively.[6] The energy is found by integrating the square of the trace over the time window.

With these values for R_1 and R_2, the corresponding values of g_o and B_o can be found using Figure 3-1. This paper uses an alternative method to find g_o and B_o from R_1 and R_2. A table of values was calculated by calculating the Green's function from different values of B_o, g_o, and r. The two dimensional, radiative transfer Green's function, GF, that was used in this paper is

$$GF(t) = \frac{1}{4\pi Dt}\left(1 - \left(\frac{r^2}{c^2t^2}\right)\right)^{-.5} exp\left(\frac{c}{2D}(c^2t^2 - r^2)^{.5} - ct\right); \qquad (3.8)$$

where D is the diffusion coefficient, r is the distance between the source and the receiver, c is the energy velocity of the medium, and t is the time.[19] Given B_o, g_o, and r, the values for E_1 and E_3 were calculated from the Green's function. The table of values created by this method was then used to find B_o and g_o for values of r, E_1, and E_3 estimated from the data.

3.3 Applications of MWTLA

MWTLA has been successfully used to find measurements of scattering and intrinsic attenuation in a number of different types of geologic regions. Table 3.1 summarizes some of these results for regions that are volcanic like the Cianten Caldera and for regions that are different from the Cianten Caldera. The values g_o and B_o that are shown are for frequencies closest to 4 to 6 Hz, the frequencies that dominate the Awibengkok dataset as shown in Figure 4-5. The papers listed in this table are discussed in more detail below.

Fehler et al. 1992 developed MWTLA in order to be able to separate the effects of intrinsic attenuation and scattering. They examined three frequency bands that ranged from 1 to 8 Hz for data from the Kanto-Tokai region of Japan and found regional values for both the scattering coefficient and the intrinsic attenuation coefficient.[6] Mayeda et al. 1992 applied MWTLA to three geologically different re-

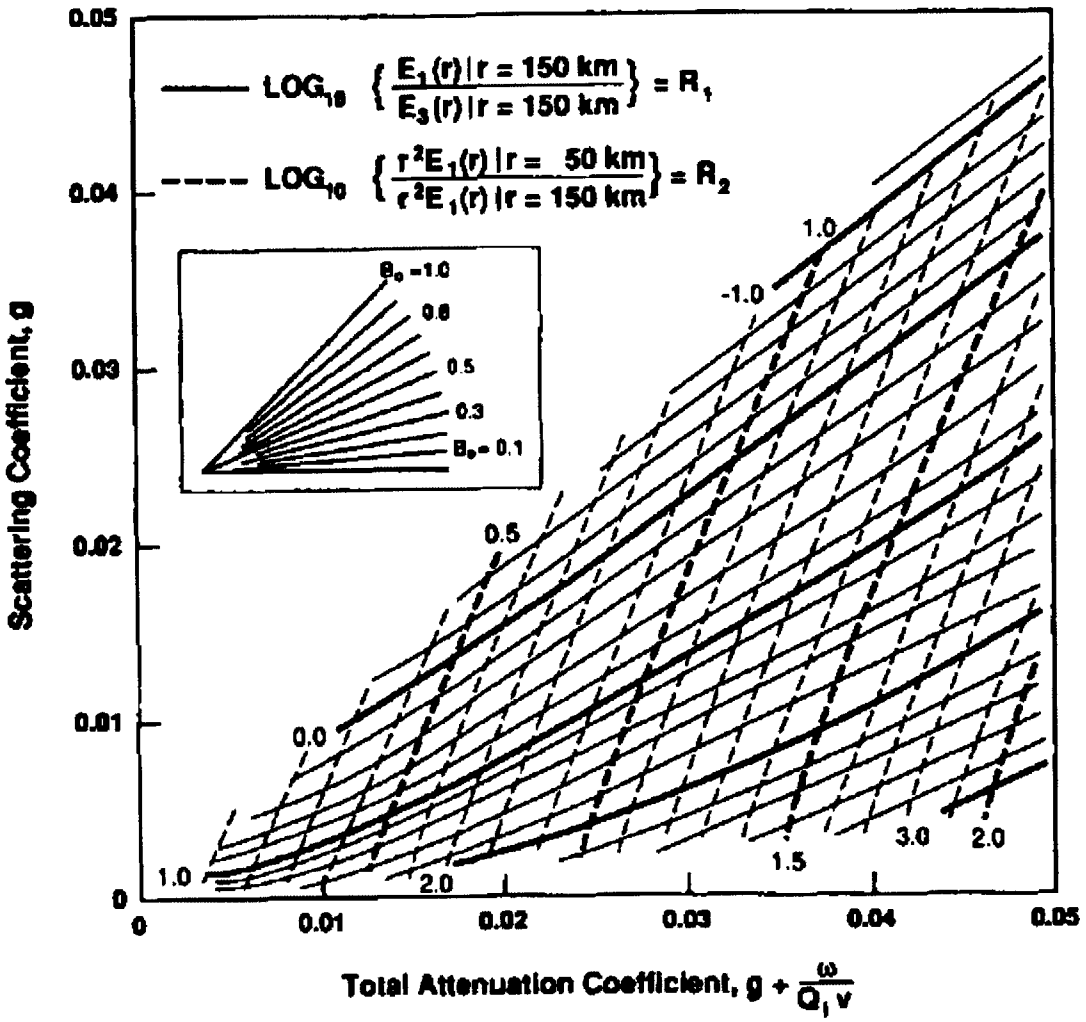

Figure 3-1: This figure shows the graphical relationship between R_1, R_2, g_o, and the total attenuation coefficient. For specified values of R_1 and R_2, the scattering coefficient, g_o, and the total attenuation coefficient can be found. From these two numbers, the seismic albedo, B_o, can be obtained. This image was taken from Fehler et al., 1992.[6, p. 796]

Author	Region	g_o [km^{-1}]	B_o [ ]	Frequency [Hz]
Fehler et al.[6]	Kanto-Tokai, Japan	0.01	0.04	3
Mayeda et al.[16]	Hawaii	0.029	0.98	3
Mayeda et al.[16]	Long Valley	0.41	0.74	3
Mayeda et al.[16]	Central California	0.022	0.63	3
Jin et al.[12]	Southern California	0.01	-	3
Leary and Abercrombie[14]	Cajon Pass borehole	0.0021	0.09	7
Adams and Abercrombie[2]	Cajon Pass borehole	0.0048	0.19	10
Bianco et al.[3]	Southern Apennines	0.0027	0.13	3
Dutta et al.[5]	South-Central Alaska	0.0024	0.22	3
Carcol and Sato[4]	Japan	0.002 to 0.05	0.165 to 0.408	2
Yamamoto and Sato[28]	Asama Volcano, Japan	0.71	-	12

Table 3.1: This figure shows the results from various studies of MWTLA in different geologic regions. Volcanic regions like the Cianten Caldera tend to have larger values of g_o and B_o larger than 0.5 because the layered composition of volcanoes makes them very heterogeneous.

gions: the volcanic island of Hawaii, the Long Valley Caldera in Long Valley, and central California along the San Andreas Fault. They analyzed seismic signals for six frequency bands between 1.5 Hz and 15 Hz, double the range of Fehler et al. 1992.[16] Jin et al. 1994 expanded the range of frequencies used for MWTLA up to 32 Hz using TERRAscope data from southern California.[12] Leary and Abercrombie 1994 applied MWTLA to data recorded by one receiver at the Cajon Pass borehole for frequencies as high as 160 Hz.[14] Adams and Abercrombie 1998 reevaluated the same area with more sources and receivers and a frequency range of only 125 Hz. Although Adams and Abercrombie obtained slightly different values for g_o and B_o than Leary and Abercrombie, the error bars of the study by Adams and Abercrombie includes the values found by Leary and Abercrombie.[2] Bianco et al. 2002 analyzed traces in the Southern Apennines in six bands at low frequencies from 1 to 12 Hz. They found that intrinsic absorption dominated the sedimentary areas, and scattering dominated the volcanic areas on the edges of their study. For the 2 to 4 Hz band in the region dominated by intrinsic attenuation that is the main focus of the study, both B_o and g_o area much smaller than other values from less sedimentary rocks.[3] Dutta et al. 2004 examined traces with much higher magnitudes from 3.0 to 6.3 in south-central Alaska for frequencies from 0.6 to 10 Hz.[5] Carcol and Sato 2010 examined the variation in the g_o and B_o across Japan and were able to mapped the spatial distribution of g_o and α for 1 to 32 Hz.[4] Yamamoto and Sato 2010 used an active seismic experiment at Asama Volcano, Japan with very dense observations in order to examine both P-waves and S-waves and the conversions between the two modes.[28]

In general, these studies show that more volcanic regions tend to have larger values for g_o. The relative amount of intrinsic attenuation can vary depending on the specific region, so the values for B_o in volcanic areas can vary more. However, B_o is generally larger than 0.5, so more of the energy in the direct arrival of the wave is attenuated by scattering rather than intrinsic attenuation. This agrees with what would be predicted from the geology of volcanoes since they are very heterogeneous with complicated internal structures.

MWTLA has developed from only being able to give a regional estimate of the scattering coefficient and the seismic albedo from S-waves. This method can now map the changes in g_o and B_o across a region given a dense enough distribution of sources and receivers. It can also account for P-waves and mode conversions. The ability to separate the intrinsic attenuation from the scattering attenuation is invaluable and provides a new way to examine the interior of the Earth.

Chapter 4

Results

In this chapter, the results for the seismic albedo, B_o, and the scattering coefficient, g_o, are shown from applying two dimensional MWTLA first to a synthetic two dimensional acoustic dataset and then to two orthogonal planes of sources and receivers from the Awibengkok microseismic dataset.

The figures that are used to convey the results for B_o and g_o are all created in the same manner. The two dimensional plane of sources and receivers is broken into cells. These cells were 0.05 km wide and 0.05 km deep for the synthetic acoustic data and 0.1 km wide and 0.1 km high for the microseismic data. B_o and g_o are calculated for each path joining a source and receiver pair. B_o and g_o are put into every cell on the path between that source and receiver along with the length of the path in that cell. Once all of the paths are calculated, the weighted averages of both B_o and g_o are taken for each cell based on the path length in each cell. These weighted averages for B_o and g_o are the values that are shown in each cell of the figures. This is similar to the method that is used for traveltime tomography.[20, Ch. 5]

4.1 Synthetic Acoustic Data

The locations of the sources and receivers used to construct the seismic traces used for this case are described in Section 2.1. Figure 4-1, Figure 4-2, and Figure 4-3 were created using a subset of this dataset including line of receivers close to the surface

and two pairs of sources approximately beneath the midpoint of the line of receivers. One pair of sources is at 1.9 km deep and the other pair of sources is at 5.6 km deep. Finding B_o and g_o requires sources at two different distances from the receiver, so the resulting values for B_o and g_o are interpreted as the value between the nearer source and the receiver. The radiating pattern of lines from the shallow source is an artifact the creation of the figure, since values are assigned to cells on the path between a certain source and receiver pair.

Figure 4-1 shows the calculated values of g_o for the synthetic acoustic dataset. There is very little variation in the values of g_o across this figure. The values of g_o range from 1.6 km^{-1} to 2.0 km^{-1}. The average value of g_o is 1.77 km^{-1}, which is close to the expected value of g_o estimated from the model of 1 km^{-1}.

Figure 4-2 shows the calculated values of B_o for the synthetic acoustic dataset. The values of B_o range from 0.65 to 0.75 and vary little over this figure. This is consistent with the constant artificial decay that was imposed on the waveforms. The artificial decay that was applied to the waveforms as a substitute for the intrinsic attenuation, α, was 0.3 km^{-1} as described in Section 2.1. Assuming g_o is equal to the estimated value of 1 km^{-1}, Equation 3.1 gives the expected value of B_o for the model be approximately 0.77. This matches the average value of B_o in Figure 4-2 of 0.71.

Figure 4-3 shows the number of times a cell in the figure is on a path between a source and receiver. Most of the cells far from the sources are in the figure are only sampled once or twice. Cells with larger values are closer to the receivers where more paths overlap.

These results for B_o and g_o are typical results for the synthetic acoustic dataset. These values agree with the expected results, so only these this case is shown in detail.

4.2 Microseismic Data

The data used for this case is described in Section 2.2.

Figure 4-4 shows a typical trace from the microseismic dataset. This trace was normalized by dividing by the maximum value of the absolute value of the trace.

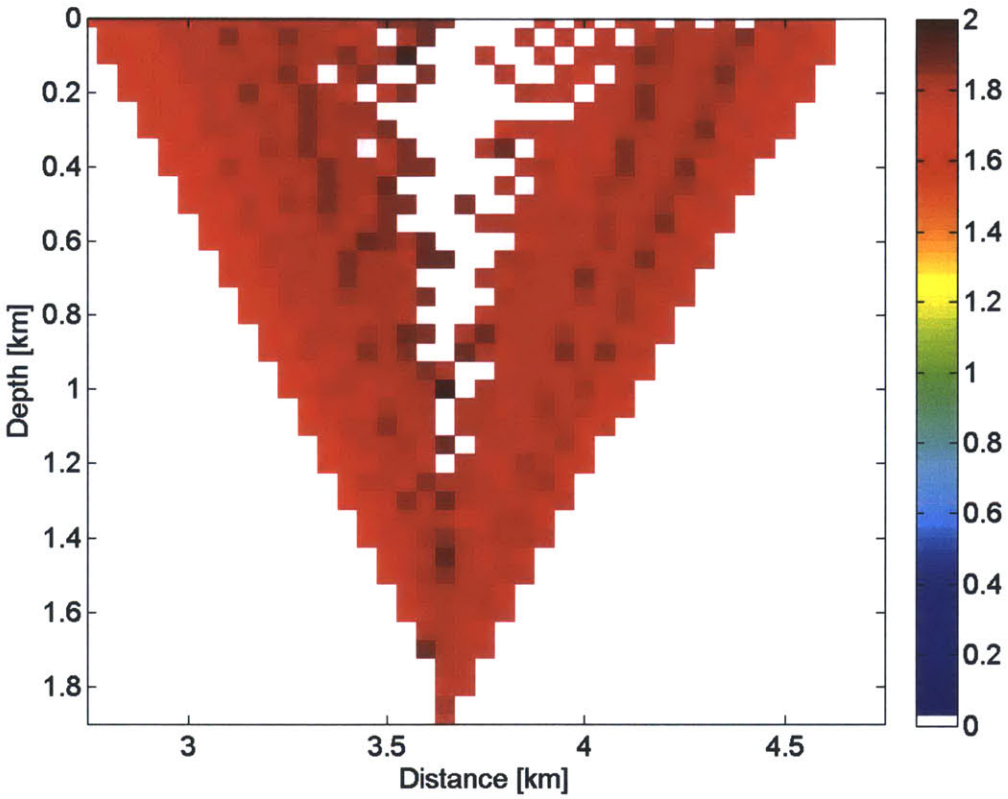

Figure 4-1: This figure shows g_o for the synthetic acoustic data. The colorbar is in units of inverse kilometers. The values for g_o across this figure range from 1.6 km^{-1} to 2.0 km^{-1} and are approximately uniform. The radiating pattern of lines from the shallow source is an artifact of the manner in which the figure was made. The average value of g_o is 1.77 km^{-1}, which is close to the estimated value of 1 km^{-1}.

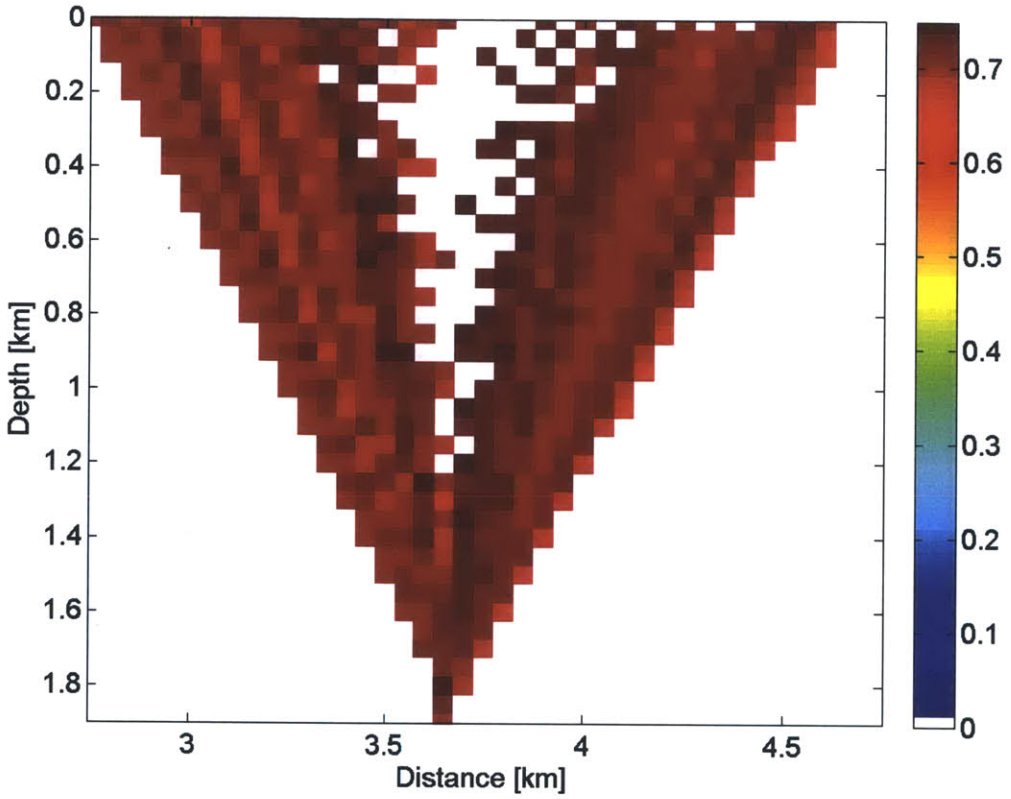

Figure 4-2: This figure shows B_o for the synthetic acoustic data. The colorbar is unitless, and B_o ranges from 0 to 1. The values for B_o across this figure range from 0.65 to 0.75 and are approximately uniform. The radiating pattern of lines from the shallow source is an artifact of the manner in which the figure was made. The average value of B_o is 0.71, which agrees with the expected value of 0.70.

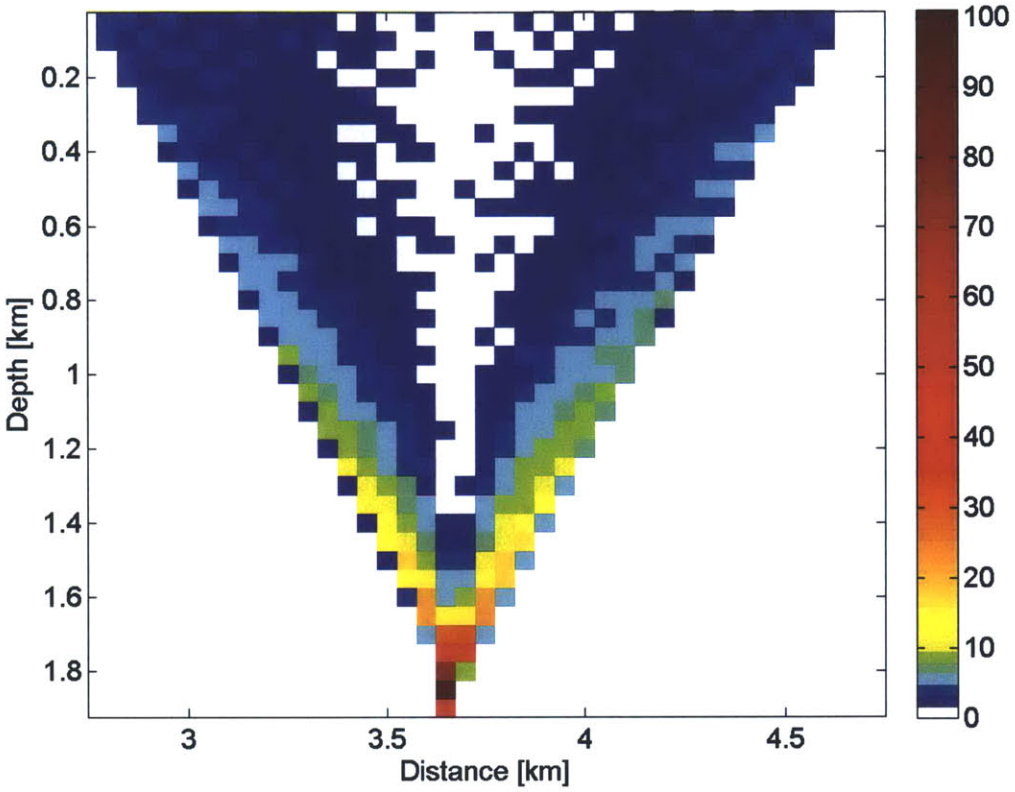

Figure 4-3: This figure shows the number of times a path from a source to a receiver in the synthetic acoustic data traveled through any cell in the figure. Most of the cells far from the sources are in the figure are only sampled once or twice. Cells with larger values tend to be along the path between a cluster of sources and a receiver and near the receivers in general.

This particular trace is the east component of receiver 8 from event 3271 located at 675.1 km north, 9252.8 km east, and 1.7 km deep. Figure 4-5 shows the Fourier transform of this trace. Other traces from this dataset have frequencies similar to the frequencies seen in this trace.

The maximum value of Figure 4-5 occurs at 4.42 Hz, the strongest frequency of the seismic trace in Figure 4-4. The full-width, half-height peak frequencies occur between 3.5 Hz and 6.5 Hz. The most prominent wavelengths of this seismic trace range from 539 m to 1 km, assuming an average background velocity of 3.5 km/s. The range of wavelengths contained within the seismic trace are important because they show the scale of a heterogeneity required to scatter the seismic wave. A heterogeneity much larger than the wavelength will cause the wave to turn slowly rather than scatter. A heterogeneity that is much smaller than the wavelength will alter the perceived properties of the medium that the wave travels through. A heterogeneity that is approximately the same size as the wavelength will cause the wave to scatter.[22, Ch. 3] Consequently, scattering should be the dominant mechanism of attenuation if the heterogeneities are on the scale of the wavelength of the seismic traces, approximately 0.5 to 1 km.

4.2.1 Cianten West to East Results

MWTLA was applied to the waveforms from the west to east plane of sources and receivers to find values for g_o and B_o. The results of this analysis are presented in this section.

Figure 4-6 shows the values for g_o that are derived from the north component of the receivers on the west to east plane of sources and receivers. There is no discernible pattern or trend in the variation in values of g_o. While there are a few scattered larger values of g_o that range up to 7.4 km^{-1} and smaller values as low as 0.2 km^{-1}, the vast majority of the values in this figure are in the range of 0.5 to 1.2 km^{-1}. The consistency of values across this figure shows that the values of g_o do not change across the length of this section, especially since measured values for g_o range over several orders of magnitude. In this figure, the average value of g_o is 1.10 km^{-1}. This

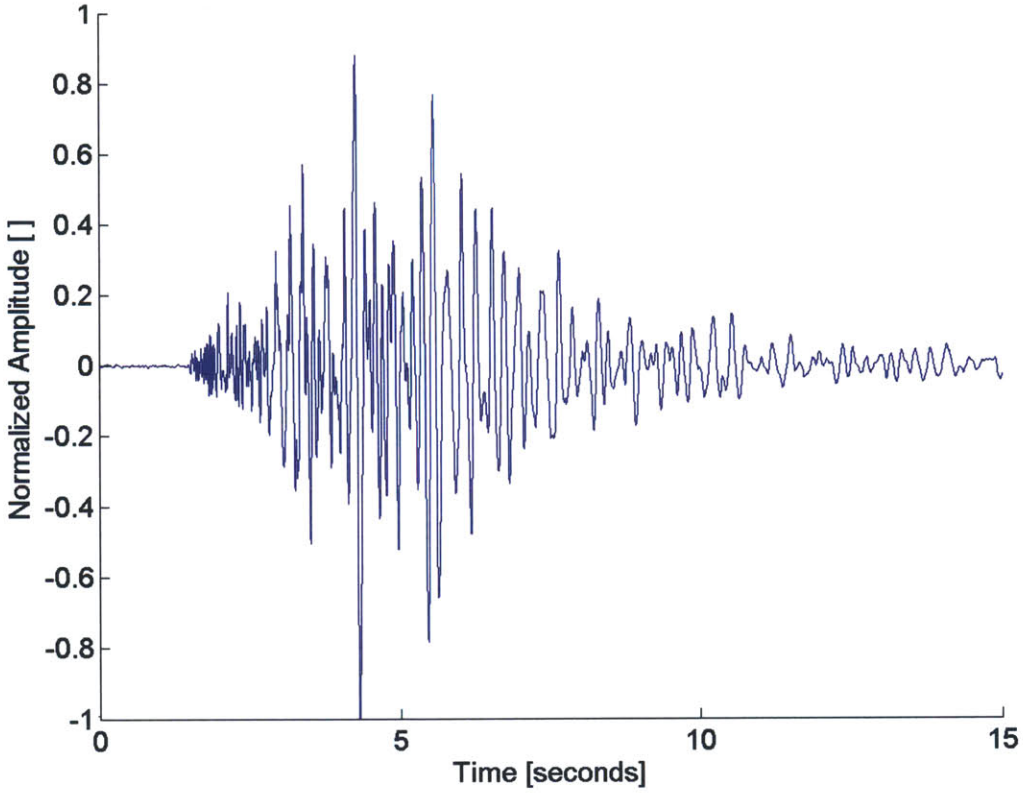

Figure 4-4: This figure shows the first 15 seconds of a normalized seismic trace from the microseismic dataset. This is event 3271 as it was recorded on the east component of receiver 8. This seismic trace is typical of the waveforms seen in this dataset.

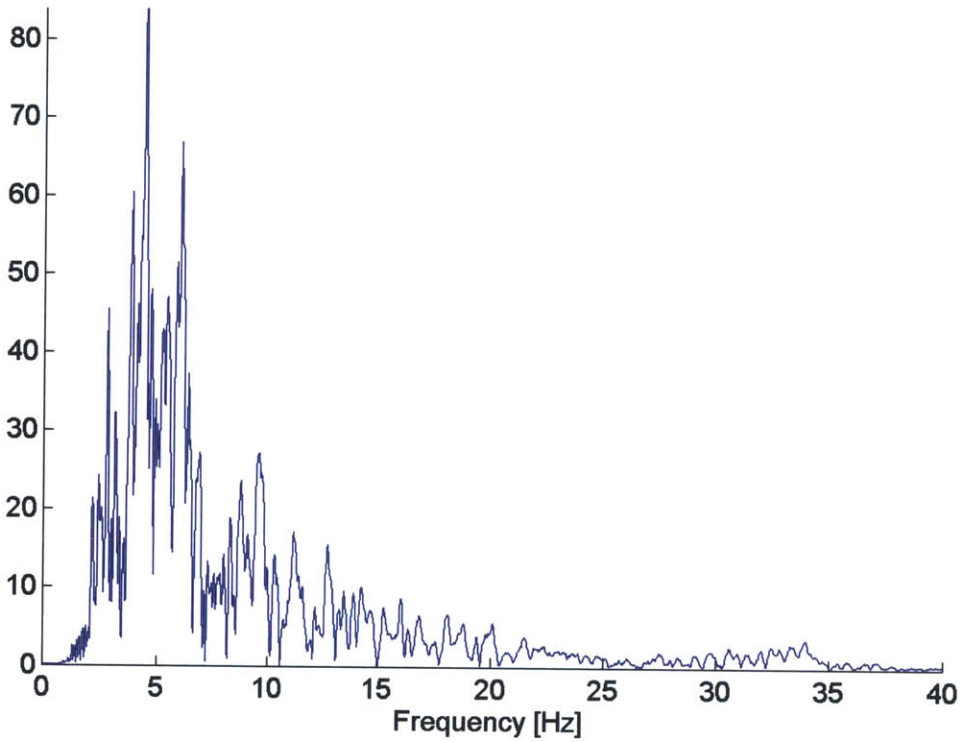

Figure 4-5: This figure shows the spectrum of the seismic trace in Figure 4-4. The maximum frequency occurs at 4.42 Hz. The full-width, half-height peak frequencies occur between 3.5 Hz and 6.5 Hz, which corresponds to wavelengths of approximately 0.5 to 1 km. This is consistent with the other waveforms for the microseismic dataset. Although there are contributions from frequencies outside of this range, the dominant length scale at which these waveforms would scatter is approximately on the scale of 0.5 to 1 km.

value is agrees with the value of g_o of 1 km^{-1} for volcanic rocks from Yamamoto and Sato 2010.[28]

Figure 4-7 shows the values for g_o that are derived from the east component of the receivers on the west to east plane of sources and receivers. This figure closely resembles Figure 4-6 in both the values of g_o and the distribution of those values. The values of g_o in this figure range from 0.3 km^{-1} to 7.1 km^{-1}, with a mean value of 1.05 km^{-1}. Both the east and the north transverse component of the receiver for g_o on the west to east plane give very similar calculated results. The transverse component that is chosen also has very little affect on all of the other results for B_o and g_o in both the west to east plane and the south to north plane. The vertical component of the receivers were not examined as we were dealing primarily with the S-wave. As a result, only the figures for the north component will be shown from now on.

Figure 4-8 shows the values for B_o derived from the north component of the receivers on the west to east plane of sources and receivers. Two distinct values for B_o can be seen in this figure. The paths originating with the sources on the eastern side of the figure have an average B_o value of approximately 0.8. The paths originating with the sources on the western side of the figure have an average B_o value of approximately 0.6. The overlap between the two sides occurs in the cluster of sources around 679 km. The Maura fault intersects this plane at the surface at 679.2 km, although the dip of the fault is unknown. The error in the location of these events ranges from tens to hundreds of meters.[17] This uncertainty in the locations of the sources could be consistent with the idea that the paths with different values of B_o correspond to differences in the material on either side of the fault.

Figure 4-9 shows the number of times each cell is sampled in the west to east plane of sources and receivers for the north component of the receivers on that plane. Cells are sampled more often closest to the receivers where more source to receiver paths overlap. Cells are also samples more often when they are on the path between a dense cluster of sources and a receiver. The largest cluster of receivers in this figure is the cluster around 679 km. Most of the cells in this figure are only sampled once or twice, but a few are sampled as many as 61 times. Consequently, there is a large

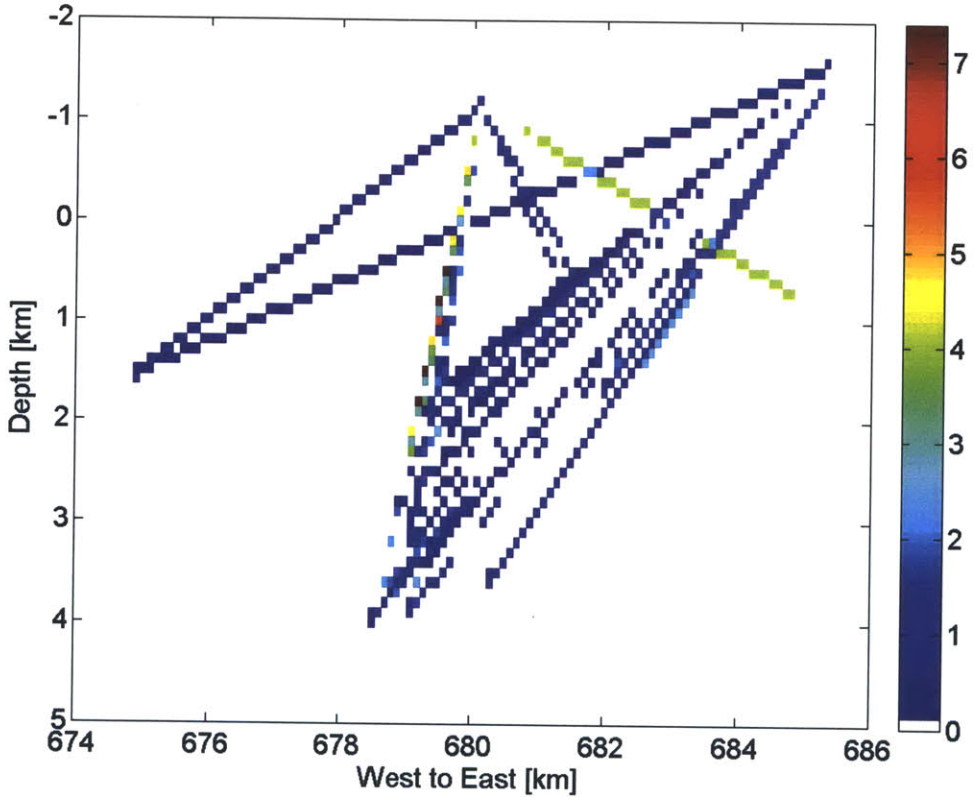

Figure 4-6: This figure shows g_o for the west to east plane for the east component of the seismogram. The colorbar is in units of inverse kilometers. The values for g_o across this figure are approximately constant and show no distinct pattern. The average value of g_o in this figure is 1.10 km^{-1}.

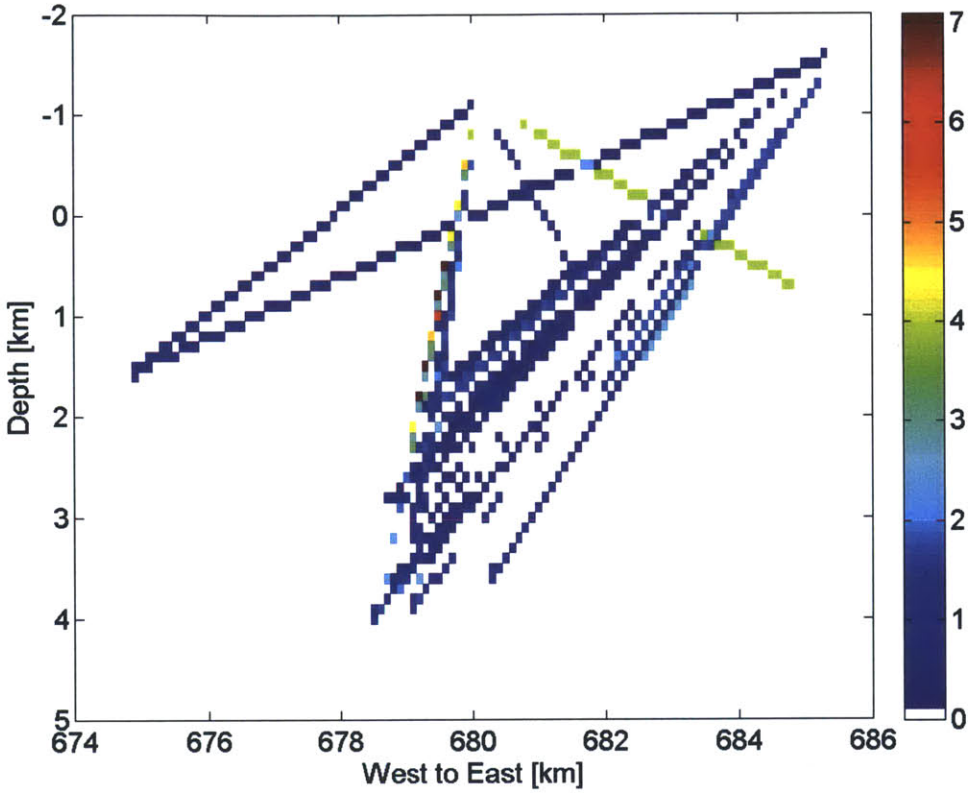

Figure 4-7: This figure shows g_o for the west to east plane for the north component of the seismogram. The colorbar is in units of inverse kilometers. Similar to Figure 4-6, the values for g_o across this figure are approximately constant and show no distinct pattern. The average value of g_o in this figure is 1.05 km^{-1}. Since the results from the east and north components of the receiver are so similar here and in all of the remaining results, only the north component will be examined from now on.

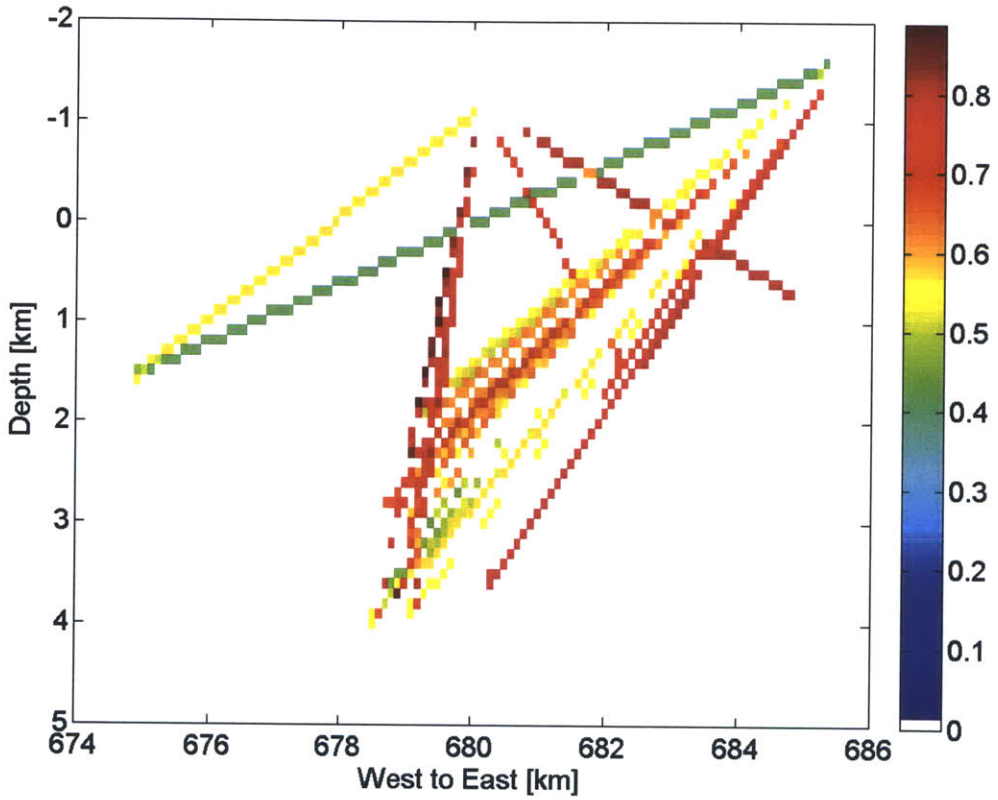

Figure 4-8: This figure shows B_o for the west to east plane for the north component of the seismogram. The colorbar is unitless, and B_o ranges from 0 to 1. Most values of B_o are near either 0.6 or 0.8. The larger values of B_o tend to be from sources on the east side of the figure and the smaller values of B_o tend to be from the west side of the figure with some overlap in the central cluster of sources. The difference may be caused by differences in the attenuation coefficient on different sides of the Maura fault.

variation in the number of contributions to the value of B_o or g_o for any particular cell.

The cells that are only sampled a few times will be strongly influenced by whichever source to receiver paths happen to cross that cell. The addition of more paths and especially more intersecting paths through each cell allows any single extreme value that may be influenced by noise to be averaged out. This redundancy of data increases the confidence of the results as opposed to being determined from a single source to receiver waveform. The concentration of most of the multiply sampled cells into a single line in this distribution of source and receiver paths would make it difficult to draw conclusions from the distribution of g_o and B_o without strong trends like the trends found in this results from this dataset.

4.2.2 Cianten South to North Results

MWTLA was applied to the waveforms from the south to north plane of sources and receivers to find values for g_o and B_o. The results of this analysis are presented in this section.

Figure 4-10 shows the values for g_o derived from the north component of the receivers on the south to north plane of sources and receivers. The values of g_o range from 0.2 km^{-1} to 3.3 km^{-1}, but most of the values for g_o in this figure are closer to the average value of 1.25 km^{-1}. This value of g_o is in agreement with the value of g_o of 1 km^{-1} by Yamamoto and Sato 2010 for volcanic rocks.[28] The values for g_o across this figure are approximately constant and show no distinct pattern, especially since measured values of g_o range over several orders of magnitude. There is little variation in g_o across this section.

The average value for g_o of 1.25 km^{-1} in Figure 4-10 for the south to north plane is slightly higher than the average value for g_o of 1.10 km^{-1} in Figure 4-7 for the west to east plane. Note that the colorbar on Figure 4-10 is different from the colorbar on Figure 4-7. The maximum of Figure 4-10 is 3.3 km^{-1} and the maximum of Figure 4-7 is 7.1 km^{-1}, so specific colors do not correspond to the same values.

Figure 4-11 shows the values for B_o derived from the north component of the

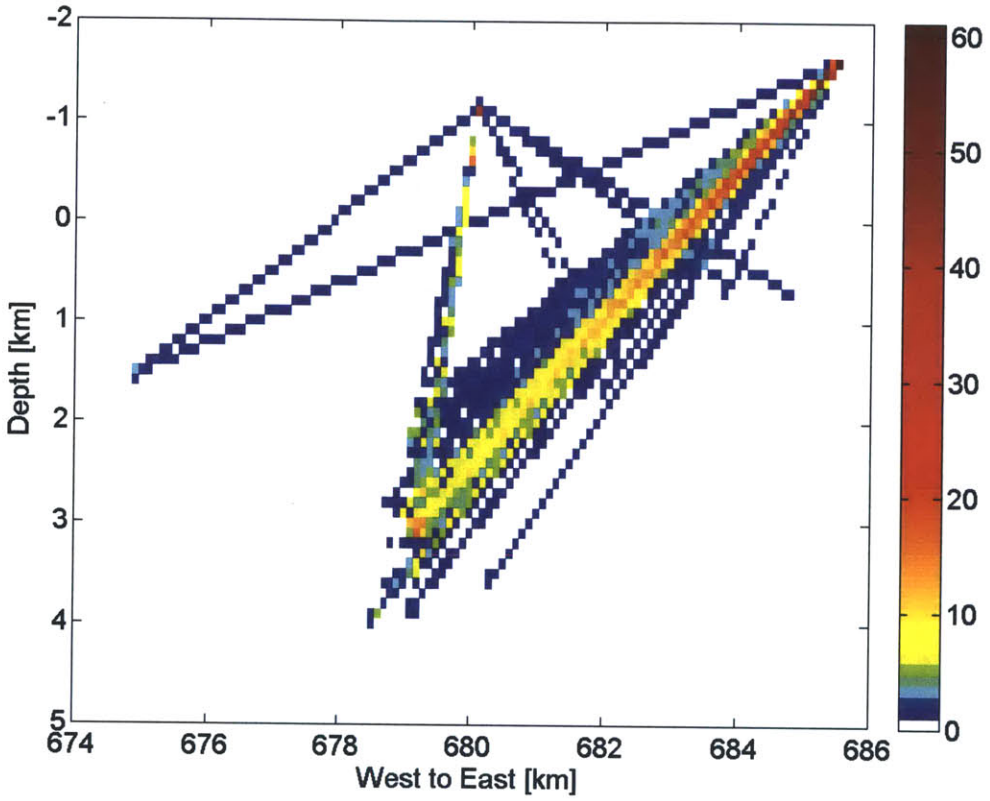

Figure 4-9: This figure shows the number of times a path from a source to a receiver traveled through any cell in the west to east plane for the north component of the seismogram. Most of the cells in the figure are only sampled once or twice. The exception is are the paths from the dense cluster of sources at approximately 4 km depth and 679 km east to the receiver at 686 km east. Since the most of the highly sampled cells in this figure occur on a single line, the quality of the results from this distribution of sources and receivers could be difficult to determine without a strong pattern.

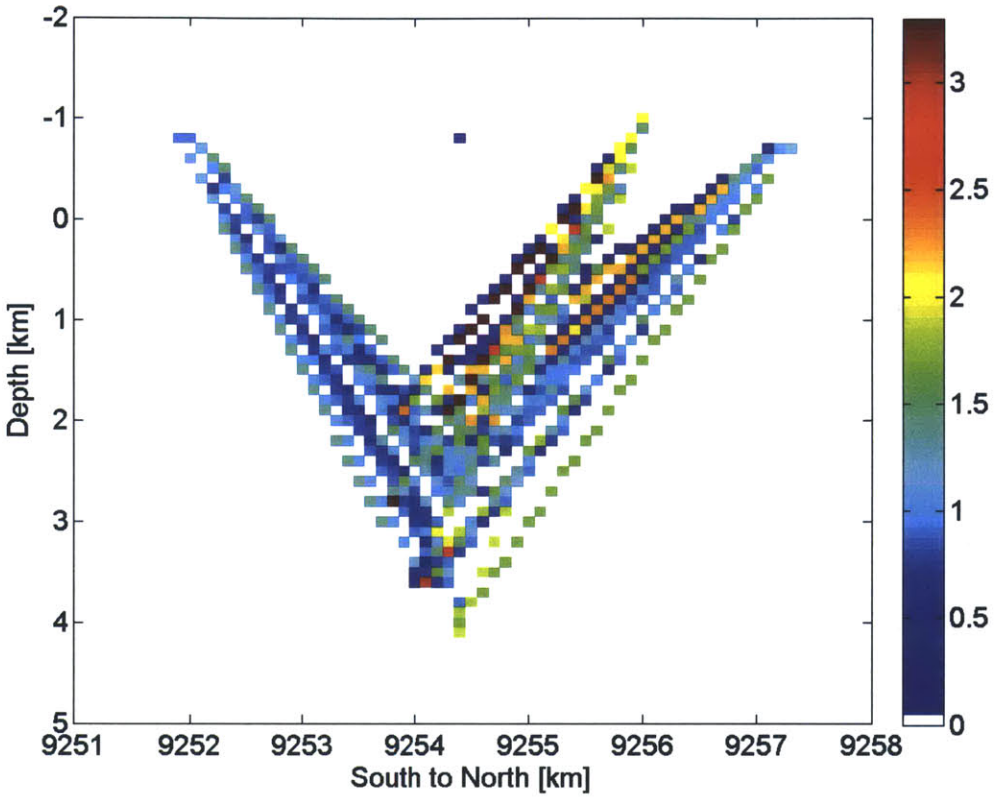

Figure 4-10: This figure shows g_o for the north-south plane for the north component of the seismogram. The colorbar is in units of inverse kilometers and has a different range than the previous figures for g_o. The values for g_o across this figure are approximately constant and show no distinct pattern. The average value of g_o is 1.25 km^{-1}.

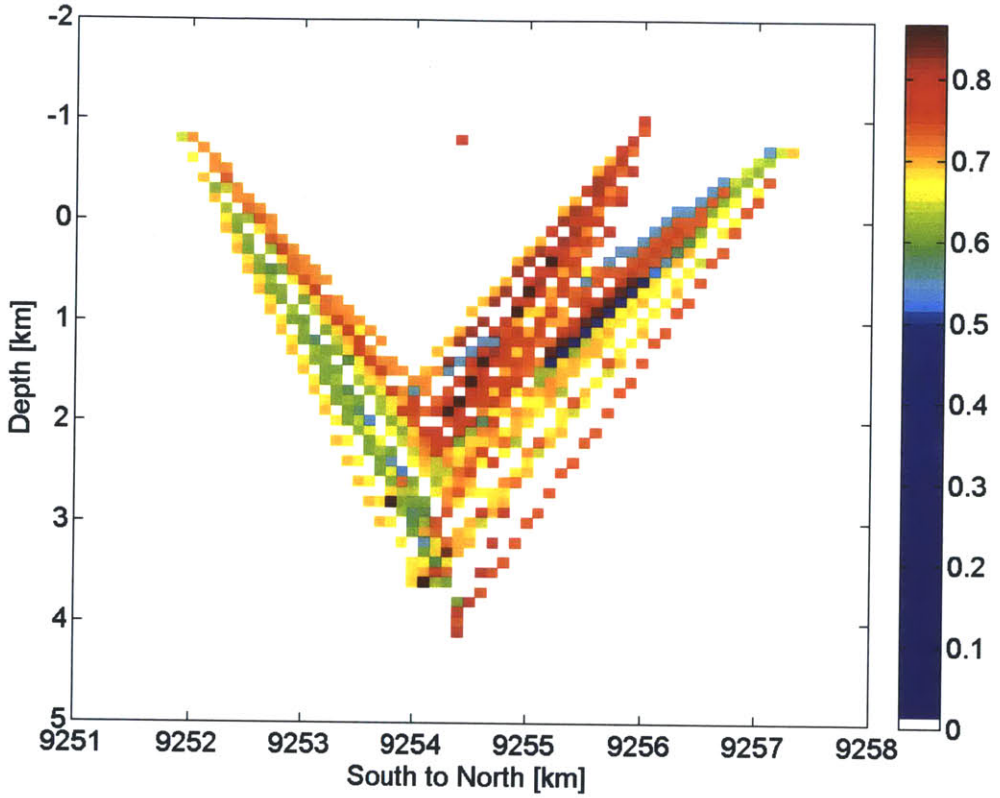

Figure 4-11: This figure shows B_o for the north-south plane for the north component of the seismogram. The colorbar is unitless, and B_o ranges from 0 to 1. Most values of B_o are near 0.65 or 0.8. The smaller values of B_o tend to be to either the northernmost receiver or the southernmost receiver. The larger values of B_o tend to be from the cluster of sources to the middle receiver at 9256 km. This receiver is located within the Cianten Caldera. The Maura fault intersects this cross section at 9254.3 km.

receivers. The values for B_o in this figure range from 0.43 to 0.87. However, most of the values are close to either 0.65 or 0.8. Most of the lower values of B_o are found along the path between the cluster of sources around 9254 km and either the southernmost receiver located at approximately 9252 km or northernmost receiver located at approximately 9257 km. Most of the larger values of B_o are along the paths from the cluster of sources to the middle receiver, located at approximately 9256 km. This middle receiver is the only receiver that is located within the Cianten Caldera. The Maura fault intersects this cross section at 9254.3 km.

Figure 4-12 shows the number of times a path traveled through each cell in the

south to north plane of sources and receivers for the north component of the receivers in that plane. Similarly to Figure 4-9, the cells that were sampled the largest number of times are either near the receivers or between the largest cluster of sources and each receiver. In this plane of sources and receivers, most of the sources lie in a single cluster, so many of the paths between individual sources and receivers overlap. However, most of the cells in the Figure 4-12 are sampled less than 3 times. With the lack of intersecting paths in this distribution of source to receiver paths, it would be difficult to draw conclusions from the distribution of g_o and B_o without strong trends like the trends found in this results from this dataset.

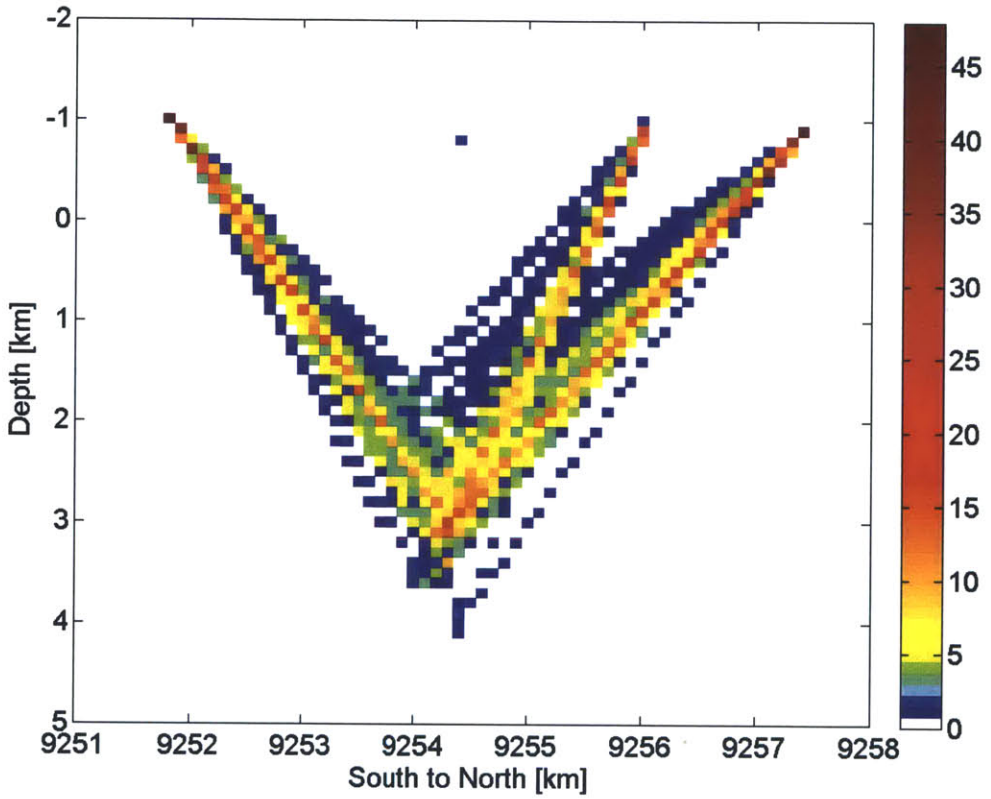

Figure 4-12: This figure shows the number of times a path from a source to a receiver traveled through any cell in the south to north plane for the north component of the seismogram. Most of the cells in the figure are only sampled a few times except along the path from the center of the cluster of sources at 3 km depth to each of the three receivers. With only three lines of highly sampled areas, the quality of the results from this distribution of sources and receivers could be difficult to determine without a strong pattern.

Chapter 5

Discussion

The implications of the results for the intrinsic attenuation coefficient, B_o, and the scattering coefficient, g_o, that are shown in Chapter 4 are examined in this chapter for both the synthetic acoustic dataset and the Awibengkok microseismic dataset. Potential areas for further investigation with the Aweibengkok dataset are also discussed.

5.1 Synthetic Acoustic Data

The two dimensional synthetic acoustic dataset was created in order to test the MWTLA code and explore some of the limitations of the process with a dataset that did not have the complications and uncertainties associated with real seismic signals. The synthetic waveforms were designed to have a value for intrinsic attenuation, α, of 0.3 km^{-1} and estimated to have a value for the scattering coefficient, g_o, of 1 km^{-1}. This gives the expected value of B_o of 0.77. Figure 4-2 has an average value of B_o of 0.71, which is close to the expected value of 0.77. Figure 4-1 has an average value of g_o of 1.77 km^{-1}, which is close to the expected value of 1 km^{-1}. This is a relatively small difference in g_o considering that reasonable values for g_o range over several orders of magnitude. The values for B_o and g_o calculated by MWTLA agree with the expected results for the synthetic acoustic model.

The agreement of the results from the application of MWTLA to the synthetic

acoustic dataset with the values predicted based on the construction of the model gives confidence in the MWTLA code and MWTLA itself. This agreement remains true for the two other velocity models in the synthetic acoustic dataset. Other variations on the specific setup in Figures 4-2, 4-1, and 4-3, were also examined where variables such as the depths of sources, the numbers of sources, the distribution of receivers, the number of receivers, and the density of receivers were changed within the dataset as described in Section 2.1. Despite these changes, the general agreement between the expected values and the calculated values did not change. These results support the robustness of MWTLA.

5.2 Microseismic Data

Two dimensional MWTLA was used on the Awibengkok microseismic dataset to find the distribution of values for B_o and g_o. The north and east components of the receivers both gave approximately the same image for the same variable. The shear component that was chosen does not significantly alter the resulting figures. The north component of the seismogram will be used for discussion in this section.

There are several significant geological features in the region of the microseismic dataset that are described in detail in Section 1.3. The Cianten Caldera is a cylindrical structure that is less than 5 km across and is separated from the active Awibengkok goethermal field by the Maura fault. The Maura Fault is an impermeable fault that trends north-northeast with an unknown dip between the Awibengkok field and the Cianten Caldera. The fault crosses the west to east plane at 679.2 km and the south to north plane at 9254.3 km. There are several sets of parallel faults and joints caused by regional stresses from the nearby active subduction zone. The Rhyodacite Marker is an anisotropic smectite clay layer that extends over both the Awibengkok field and the Cianten Caldera. This is the impermeable cap of the Awibengkok geothermal reservoir. Drilling has confirmed that temperatures are lower in the Cianten Caldera and some of the fractures have been filled by precipitants.[23]

More subtle variables that affect the signal include anisotropy and attenuation.

Anisotropy is affected by strain, stress, temperature, pressure and volatile content.[15] Intrinsic attenuation primarily comes from the motion of water within pores and fractures in the rock. Intrinsic attenuation does happen within the rock itself, however the movement of water is a much more efficient way to dissipate heat than the friction caused by shear waves within a rock, so the majority of the energy lost to intrinsic attenuation is lost in the presence of water.[20, Ch. 7] Scattering attenuation depends on the frequency of the wave because waves are best scattered by heterogeneities on the order of magnitude of their wavelength. Also, there is little difference between the effect of scattering from relatively few heterogeneities with a high reflection coefficient and scattering from many heterogeneities with low reflection coefficients.

Figure 4-5 showed that the peak frequencies found in the microseismic trace from Figure 4-4 in the dataset range from 3.5 Hz to 6.5 Hz. The corresponding wavelengths of these waves assuming a 3.5 km/s velocity is 539 m to 1 km. This is the size of the heterogeneity needed to scatter this wave.

Figures 4-7 and 4-10 both show very small variation over the extent of the data. There is also no discernible pattern or trend in either figure. Consequently, these results show that the value for g_o in the west to east plane and in the south to north plane is approximately constant in that plane. Figure 4-7 has an average value for g_o of 1.05 km^{-1}, so the mean free path, l is 0.95 km. Figure 4-10 has an average value for g_o of 1.25 km^{-1}, so l is 0.8 km. These values for g_o agree with the values for g_o of 1 km^{-1} from Yamamoto and Sato 2010.[28] The smaller value for the mean free path for the south to north plane of sources and receivers indicates that scatterers occur more frequently along the south to north plane than the west to east plane. Scatterers can be faults or joints in the medium. In Figure 1-4 shows several parallel, regularly spaced faults, especially through the Awibengkok geothermal field. These faults extend from the surface through the Awibengkok geothermal field and have sectioned the producing field into different regions that have limited hydrological contact with one another.[23]. These faults that trend to the northeast have a significant impact on the properties of the region that they divide. The west to east plane of sources and receivers does not trend directly east to

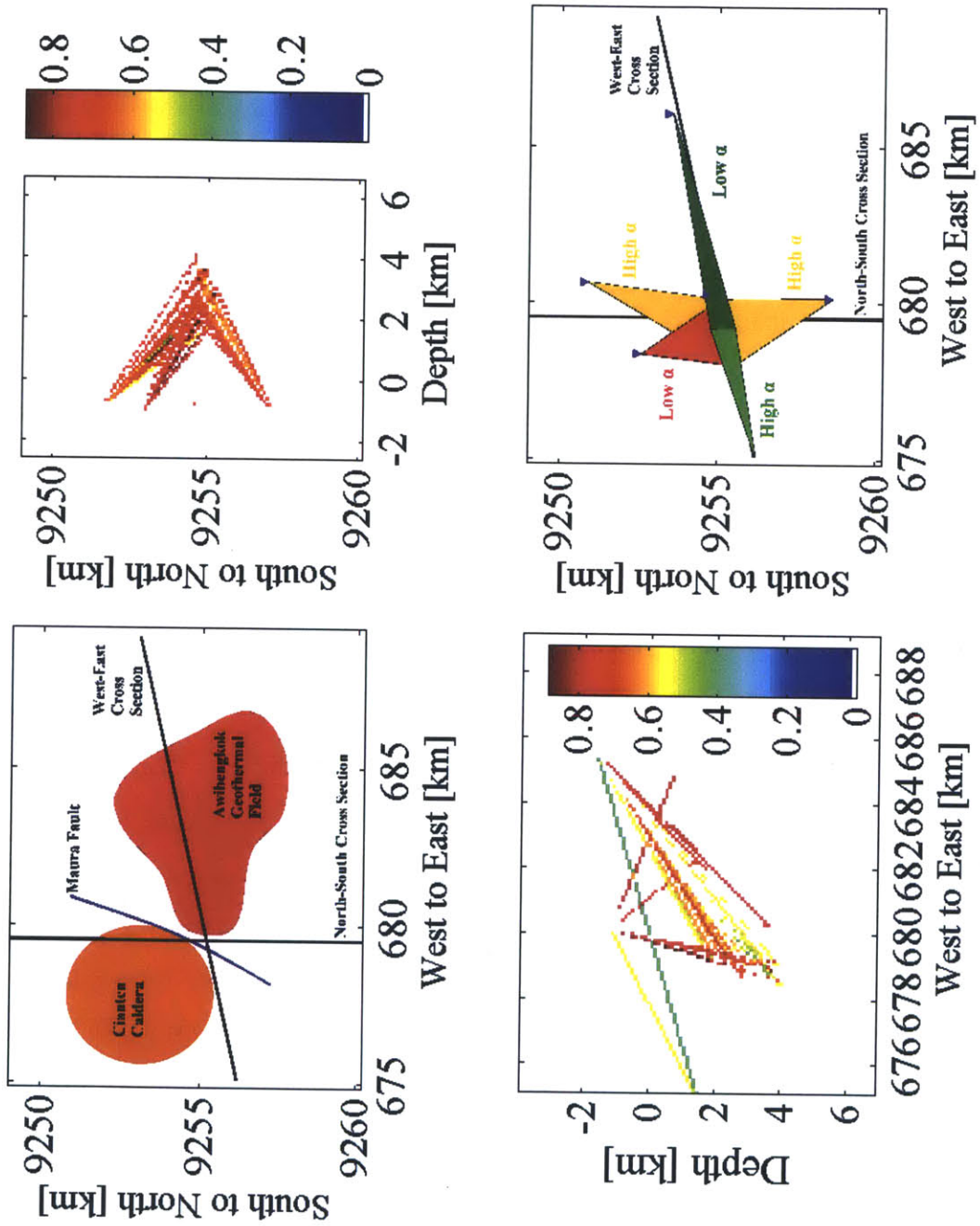

Figure 5-1: This figure shows a simplified geology map of the Awibenkok region in the upper left alongside both the figures for B_o for the Awibengkok microseismic dataset. The west to east cross section is located below the simplified geology map and the south to north cross section is located to the right of it. The colorbars are unitless. The figure in the lower left hand corner summarizes the results from both planes in a map view.

west. It trends east-northeast, so this plane of sources and receivers is more parallel to these faults. Since they are more parallel, they will intersect one another less frequently. If these faults are the primary cause of scattering for the seismic waves, then the mean free path would also increase. This would result in a distribution of g_o that would depend primarily on the direction of the path between the source and receiver since the value of l would primarily be determined by the spacing at that angle between sets of regional faults. This angular dependence could be confirmed by analyzing other planes of data or using three dimensional MWTLA with more sources and receivers.

Figure 5-1 summarizes the results of applying MWTLA to the microseismic dataset. The upper left corner is a simplified version of the geology including the Maura fault and the extent of both the Cianten Caldera and the Awibengkok geothermal field. The two black lines in the figure are the traces of the west to east cross section and the south to north cross section. The figure below the map is Figure 4-8 which shows the values of B_o on the west to east plane of sources and receivers. The figure to the right of the map is Figure 4-11 that has been rotated 90 degrees and which shows the values of B_o on the south to north plane of sources and receivers. The x axis and y axis of the simplified geology map match the corresponding axis on the figures for B_o. The figure in the lower left corner shows a map view of the results for B_o for both the west to east plane and the south to north plane stacked on top of one another. The results for the west to east plane are in green. The lower values of B_o and higher values of α in this figure are on the west side of the cluster of sources that lies at the intersection of the two cross section lines. The higher values of B_o and lower values of α are on the east. The results for the south to north plane are in red and yellow. The red region has is in the Cianten Caldera and has high values for B_o and low values of α. The yellow regions have lower values of B_o and higher values of α.

The colorbars for the figures for B_o are the same, but the values of B_o in the west to east plane of sources and receivers cannot be directly compared to the values of B_o for the south to north plane of sources and receivers. The changes in B_o between the west to east plane and the south to north plane cannot be directly interpreted as

a change in the geology of the region. B_o depends on both the scattering coefficient, g_o, and the intrinsic attenuation coefficient, α. The value of g_o in the west to east plane is different from the value of g_o in the south to north plane, so the variation in B_o is not directly related to a change in the geologic properties of the region. For this reason, each plane of sources and receivers will be considered independently.

In Chapter 4, it was determined that both figures for B_o have two distinct values for B_o.

The west to east plane appeared to be to have lower values of B_o of 0.6 on the western side of the figure and higher values of 0.8 on the eastern side of the figure. The place where these two values overlap is a cluster of sources that is divided by the Maura fault at approximately 9254.3 km. The Maura fault is one of the largest faults in the geologic map in Figure 1-4. The Maura fault is an impermeable fault that water cannot pass, indicating that the fault itself has different physical properties that the rest of the region. Since the value of g_o across the figure was determined to be constant, the variation in B_o must be due to a change in the intrinsic attenuation coefficient. Since both of the receivers that fall on the west to east plane are to the east of the fault, all of the waveforms from the western side of the figure on the other side of the Maura fault must pass through the fault. The bimodal distribution of B_o values could be explained by the Maura fault being a major source of intrinsic attenuation due to either softer material that more readily dissipates heat or the presence of an unusual amount of water. These results indicate that the Maura Fault could be having a large effect on the distribution of the intrinsic attenuation coefficient.

The south to north plane of sources and receivers saw a general trend for B_o of lower values of 0.65 between the cluster of sources and the northernmost and southernmost receivers. The paths between the cluster of sources and the middle receiver at about 9256 km has higher values for B_o of 0.8. The northernmost and southernmost receivers as can be seen in Figure 2-4 lie further to the east than the middle receiver. The middle receiver also lies within the Cianten Caldera and since the cluster of sources lies on the edge of the caldera, the path between the sources and the receivers samples the caldera along the vast majority of the path. Since the

value of g_o across the figure was determined to be constant, the increase in B_o in the Cianten Caldera must be due to a decrease in the intrinsic attenuation coefficient. The intrinsic attenuation coefficient is to a first order affected by the water content as water more easily converts seismic energy to heat than rock. A smaller value for the intrinsic attenuation coefficient could be caused by the presence of less water in the rock. The lower values of B_o in this area agree with what is known about the geology of the Cianten Caldera since the cooling of the hydrothermal system has caused minerals to precipitate into existing fractures. This displaces the water that was held in those fractures and reduced the overall amount of water in the region.

The relatively low rates of sampling indicated by Figures 4-9 and 4-12 show that the value in each cell is often only supported by one source and receiver pairing. The patterns that have resulted from the data that was analyzed is convincing, but the results would be much more robust with a larger area of multiply sampled cells.

The values obtained for g_o and B_o are similar to the values obtained by other studies[28, 13, 16] in volcanic areas that are discussed in Section 3.3. In such a heterogeneous environment as a volcano, scattering happens frequently and is the dominant form of energy loss from the direct arrival. Values for g_o are expected to be relatively large due to the small mean free path. Previous studies have obtained values for g_o of the order of 10^{-2} to 10^{0}. Since scattering is the dominant form of attenuation, values for B_o are expected to be larger than 0.5, however, specific values do vary depending on the amount of intrinsic attenuation in the region. Previous studies have found values of B_o that range from 0.7 to close to 1. The values for g_o and B_o that were obtained in this thesis agree with the expected values for this region. The Cianten Caldera has a large enough value for g_o of approximately 1 km^{-1} to be a good geothermal field, but the high value of B_o that means a low value of α indicates that there may not be enough water for an active geothermal field due to the low temperatures that have caused fractures to seal with mineral precipitants. These observations agree with what is known of the geology of the region. The Cianten Caldera would not make a good geothermal field.

The apparent continuation of the cap of the Awibengkok geothermal field to the

Cianten Caldera may not exist. The smectite clay layer found over the Cianten Caldera may be from the caldera lake sediments rather than hydrothermal alteration of ashes that forms the cap of the Awibengkok field. Alternatively, the cap could be formed by hydrothermal alteration and the Cianten Caldera may have been cut off from the Awibengkok field by the Maura fault and lost circulation of fresh hot fluids from intrusions. If the Awibengkok field and the Cianten Caldera have never been connected geothermally, then there is little likelihood that the Cianten Caldera will ever be a viable option for geothermal energy without the formation of a new intrusion. If the two regions were connected prior to the rupture of the Maura fault, there is a chance that the impermeable barrier of the Maura fault could be broken and hydrothermal activity eventually restored by a process like hydrofracing. Such an endeavor on the scale that would be required may be beyond current technology and the timescale of reheating the Cianten reservoir may be too long to be economically viable. An extension of the smectite clay layer may in a direction different than the Cianten Caldera may prove more fruitful to pursue.

5.3 Future Work

More information about the geologic characteristics of the Cianten Caldera and the Awibenkok geothermal field could be extracted from the Awibengkok microseismic dataset beyond the scope of what was investigated in this thesis. Further work with MWTLA and the Awibengkok microseismic dataset could increase confidence in the trends observed in the Cianten Caldera and the surrounding area, reveal other patterns that are not observable within the limitations of this study, and extend the geographic extent of the current results.

The amount of the data from the Awibengkok microseismic dataset that was used in this analysis was limited. The vertical component of the receivers was not examined. The dataset includes events from 2005 to 2010 distributed across the entire Awibengkok geothermal field and the surrounding areas, but the events used were limited to October 2008 when there was significant activity near the Cianten

Caldera. Utilizing more sources and receivers over a larger geographic area would increase both the redundancy of the results and the extent of the region covered. This would also allow the variables B_o and g_o to be monitored with respect to time as the Awibengkok field has been developed.

The distribution of the sources and the receivers that were selected for analysis in this thesis is well suited to a two dimensional application of MWTLA. However, a three dimensional application of MWTLA would sample much more of the geology and avoid any distortions caused by the projection of sources and receivers onto a two dimensional plane. Due to the larger volume that affected by a three dimensional analysis, more sources and receivers would be required in order to resolve the changes in B_o and g_o over the Awibengkok region.

This particular study analyzed the broadband values of g_o and B_o using the waveforms in their entirety. However, these variables can also be investigated with respect to the frequency dependence of the waveforms by filtering the waveforms to specific frequency bands. This type of analysis has been successfully conducted on different types of regions as is discussed in Section 3.3.[6, 16, 12, 14, 2, 3, 5, 4, 28]

The simplification for MWTLA of isotropic, homogeneous scattering as described in Section 3.2 is not likely to be accurate for the interior of the Earth. This is especially true in volcanic regions like the Cianten Caldera and the Awibengkok geothermal field, since the accumulation of layers of volcanic rock which forms volcanoes results in strongly heterogeneous rocks.[16] Another distribution that includes heterogeneities may be more accurate.[10] The extra degrees of freedom added by removing the homogeneous assumption would require more sources and receivers for the same resolution in order to resolve heterogeneities.

Bibliography

[1] Jorge A. Acuña, James Stiamc, Lutfhie Sirad-Azwar, and Riza Glorius Pasikki. Reservoir management at Awibengkok geothermal field, West Java, Indonesia. *Geothermics*, 37(3):332–346, 2008.

[2] D.A. Adams and R.E. Abercrombie. Seismic attenuation above 10 Hz in southern California from coda waves recorded in the Cajon Pass borehole. *Journal of Geophysical Research*, 103(B10):24257 – 70, Oct. 1998.

[3] F. Bianco, E. Del Pezzo, M. Castellano, J. Ibanez, and F. Di Luccio. Separation of intrinsic and scattering seismic attenuation in the Southern Apennine zone, Italy. *Geophysical Journal International*, 150(1):10–22, 2002.

[4] Eduard Carcol and Haruo Sato. Spatial distribution of scattering loss and intrinsic absorption of short-period S waves in the lithosphere of Japan on the basis of the Multiple Lapse Time Window Analysis of Hi-net data. *Geophysical Journal International*, 180(1):268–290, 2010.

[5] U. Dutta, N. N. Biswas, D. A. Adams, and A. Papageorgiou. Analysis of S-Wave Attenuation in South-Central Alaska. *Bulletin of the Seismological Society of America*, 94(1):16–28, 2004.

[6] Michael Fehler, Mitsuyuki Hoshiba, Haruo Sato, and Kazushige Obara. Separation of scattering and intrinsic attenuation for the Kanto-Tokai region, Japan, using measurements of S-wave energy versus hypocentral distance. *Geophysical Journal International*, 108(3):787–800, 1992.

[7] A. Frankel and L. Wennerberg. Energy-flux model of seismic coda: separation of scattering and intrinsic attenuation. *Bulletin of the Seismological Society of America*, 77(4):1223 – 51, 1987.

[8] John P. Grotzinger and Thomas H. Jordan. *Understanding Earth.* W.H. Freeman and Company, New York, Sixth edition, 2010.

[9] David P. Hill, Roy A. Bailey, and Alan S. Ryall. Active tectonic and magmatic processes beneath Long Valley Caldera, eastern California: An overview. *Journal of Geophysical Research: Solid Earth*, 90(B13):11111–11120, 1985.

[10] M. Hoshiba. Simulation of multiple-scattered coda wave excitation based on the energy conservation law. *Physics of the Earth and Planetary Interiors*, 67(1-2):123 – 36, 1991.

[11] Mitsuyuki Hoshiba. Separation of scattering attenuation and intrinsic absorption in Japan using the multiple lapse time window analysis of full seismogram envelope. *Journal of Geophysical Research*, 98(9):15809–24, 1993.

[12] Anshu Jin, K. Mayeda, D. Adams, and K. Aki. Separation of intrinsic and scattering attenuation in southern California using TERRAscope data. *Journal of Geophysical Research*, 99(B9):17835 – 48, Sept. 1994.

[13] Jim Kauahikaua. Geophysical characteristics of the hydrothermal systems of Kilauea volcano, Hawaii. *Geothermics*, 22(4):271 – 299, 1993.

[14] Peter Leary and Rachel Abercrombie. Frequency dependent crustal scattering and absorption at 5-160 Hz from coda decay observed at 2.5 km depth. *Geophysical Research Letters*, 21(11):971–974, 1994.

[15] Maureen D. Long and Paul G. Silver. Shear Wave Splitting and Mantle Anisotropy: Measurements, Interpretations, and New Directions. *Surveys in Geophysics*, 30(4-5):407 – 461, 2009.

[16] K. Mayeda, S. Koyanagi, M. Hoshiba, K. Aki, and Y. Zeng. A comparative study of scattering, intrinsic, and coda Q^{-1} for Hawaii, Long Valley, and central California between 1.5 and 15.0 Hz. *Journal of Geophysical Research*, 97(B5):6643 – 59, May 1992.

[17] Gabriela Melo, Alison Malcolm, Oleg Poliannikov, and Michael Fehler. Analysis of location uncertainty for a microearthquake cluster: A case study. Society of Exploration Geophysicists, 2012.

[18] K. R. Newcomb and W. R. McCann. Seismic History and Seismotectonics of the Sunda Arc. *Journal of Geophysical Research*, 92(B1):421–439, 1987.

[19] J. C. J. Paasschens. Solution of the Time-dependent Boltzmann Equation. *Phys. Rev. E*, 56:1135–1141, July 1997.

[20] Peter Shearer. *Introduction to Seismology.* Cambridge University Press, Cambridge, Second edition, 2009.

[21] M. L. Sorey, C. D. Farrar, G. A. Marshall, and J. F. Howie. Effects of geothermal development on deformation in the Long Valley Caldera, eastern California, 1985-1994. *Journal of Geophysical Research: Solid Earth*, 100(B7):12475–12486, 1995.

[22] Seth Stein and Michael Wysession. *An Introduction to Seismology, Earthquakes, and Earth Structure.* Blackwell Pub., Malden, MA, 2003.

[23] James Stimac, Gregg Nordaddquist, Aquardi Suminar, and Lutfhie Sirad-Azwar. An overview of the Awibengkok geothermal system, Indonesia. *Geothermics*, 37(3):300 – 331, 2008.

[24] Jim Stimac, Birean D. Sagala, and Mirzal Nur Ardhie. Geologic Map of the Cianten Caldera, Indonesia.

[25] Jim Stimac, Birean D. Sagala, and Gregg Nordquist. Salak Awibengkok - West Java: Geology and Structure Map of the Cianten Caldera, Indonesia. 2009.

[26] Ru-Shan Wu. Multiple scattering and energy transfer of seismic waves- Separation of scattering effect from intrinsic attenuation. I. Theoretical modelling. *Geophysical Journal of the Royal Astronomical Society*, 82(1):57 – 80, 1985.

[27] Ru-Shan Wu and Keiiti Aki. Multiple scattering and energy transfer of seismic waves- Separation of scattering effect from intrinsic attenuation. II. Application of the theory to Hindu Kush region. *Pure and Applied Geophysics*, 128(1-2):49–80, 1988.

[28] Mare Yamamoto and Haruo Sato. Multiple scattering and mode conversion revealed by an active seismic experiment at Asama volcano, Japan. *Journal of Geophysical Research.Solid Earth*, 115(7), 2010.

[29] Keita Yoshioka, Riza Pasikki, Indra Suryata, and Ken Riedel. Hydraulic Stimulation Techniques Applied to Injection Wells at the Salak Geothermal Field, Indonesia. In *SPE Western Regional Meeting 2009*. Society of Petroleum Engineers, Curran Associates Inc., 2009.